JCB Journal of Cell Biology

ARTICLE

The hypervariable region of atlastin-1 is a site for intrinsic and extrinsic regulation

Carolyn M. Kelly[1], Laura J. Byrnes[1], Niharika Neela[1], Holger Sondermann[1,3,4], and John P. O'Donnell[1,2]

Atlastin (ATL) GTPases catalyze homotypic membrane fusion of the peripheral endoplasmic reticulum (ER). GTP-hydrolysis–driven conformational changes and membrane tethering are prerequisites for proper membrane fusion. However, the molecular basis for regulation of these processes is poorly understood. Here we establish intrinsic and extrinsic modes of ATL1 regulation that involve the N-terminal hypervariable region (HVR) of ATLs. Crystal structures of ATL1 and ATL3 exhibit the HVR as a distinct, isoform-specific structural feature. Characterizing the functional role of ATL1's HVR uncovered its positive effect on membrane tethering and on ATL1's cellular function. The HVR is post-translationally regulated through phosphorylation-dependent modification. A kinase screen identified candidates that modify the HVR site specifically, corresponding to the modifications on ATL1 detected in cells. This work reveals how the HVR contributes to efficient and potentially regulated activity of ATLs, laying the foundation for the identification of cellular effectors of ATL-mediated membrane processes.

Introduction

Atlastins (ATLs) are large GTPases in the dynamin superfamily that catalyze the fusion of tubules in the peripheral ER to generate and maintain its polygonal structure composed of three-way junctions (Orso et al., 2009; Hu et al., 2009; Praefcke and McMahon, 2004). Dynamin-related proteins use the energy of GTP hydrolysis to carry out diverse cellular processes including fission of budding vesicles, fusion and fission of organelle membranes, and interferon-induced pathogen resistance (Praefcke and McMahon, 2004; Daumke and Praefcke, 2016). Dynamin superfamily members are comprised of several conserved structural domains including the canonical N-terminal large GTPase (G) domain, followed by a stalk-like helical bundle domain. The C terminus includes subfamily-specific features such as the transmembrane domain found in ATL (Praefcke and McMahon, 2004).

Three isoforms of ATL (ATL1–3) are found in most vertebrates, while other eukaryotes express only one analogous protein, such as dmATL in *Drosophila melanogaster* (Orso et al., 2009) or the more distant orthologue synthetic enhancer of Yop1 (Sey1p) in yeast (Hu et al., 2009). While all three mammalian isoforms retain high sequence identity and localize primarily to the reticular ER, they vary slightly in their sub-organellar localizations (Rismanchi et al., 2008; Nixon-Abell et al., 2016) and their tissue-specific expression patterns (Zhu et al., 2003; Rismanchi et al., 2008), with cooccurrence of more than one ATL isoform in tissues and cell lines as an apparent common feature (Rismanchi et al., 2008).

ATL1 was first identified as a mutational hotspot in hereditary spastic paraplegia (Zhao et al., 2001), and later ATL1 and ATL3 mutations were found associated with hereditary sensory neuropathy (Guelly et al., 2011; Fischer et al., 2014; Kornak et al., 2014). While ATL's most well-defined function is in ER membrane fusion, additional functional roles for ATLs continue to be identified and include (but are not limited to) regulating ER-phagy (Chen et al., 2019; Liang et al., 2018) and lipid droplets (Klemm et al., 2013; Falk et al., 2014); regulating the bone morphogenetic protein signaling pathway (Fassier et al., 2010; Summerville et al., 2016; Zhao and Hedera, 2013; Zhao et al., 2016); and aiding in mitotic ER morphological changes (Wang et al., 2013).

ATL is anchored to the high-curvature tubules of the peripheral ER by its wedge-like, C-terminal transmembrane domain (Hu et al., 2009; Betancourt-Solis et al., 2018), followed by a short, amphipathic helix that aids in membrane fusion (Faust et al., 2015; Liu et al., 2012). The N-terminal, cytosol-facing portion of ATL, composed of the G and middle domains,

[1]Department of Molecular Medicine, College of Veterinary Medicine, Cornell University, Ithaca, NY; [2]Cell Biology Division, Medical Research Counsil (MRC) Laboratory of Molecular Biology, Cambridge, UK; [3]CSSB Centre for Structural Systems Biology, Deutsches Elektronen-Synchrotron DESY, Hamburg, Germany; [4]Kiel University, Kiel, Germany.

Correspondence to Holger Sondermann: holger.sondermann@cssb-hamburg.de; John P. O'Donnell: odonnell@mrc-lmb.cam.ac.uk.

constitutes the protein's catalytic core. This region is necessary and sufficient for GTP hydrolysis (Wu et al., 2015; Moss et al., 2011; Byrnes and Sondermann, 2011; Bian et al., 2011; O'Donnell et al., 2017), nucleotide-dependent dimerization (Byrnes et al., 2013; O'Donnell et al., 2017), and acting as a concentration- and GTPase-dependent inhibitor of ATL-mediated membrane fusion in vitro and in cells (Bian et al., 2011; Moss et al., 2011, Wang et al., 2013). These properties have established the catalytic core's use as a proxy for the full-length protein in mechanistic and structural studies (Byrnes and Sondermann, 2011; Byrnes et al., 2013; Bian et al., 2011; Liu et al., 2015; O'Donnell et al., 2018).

A number of studies have culminated in a detailed model of ATL's catalytic mechanism (Byrnes and Sondermann, 2011; Bian et al., 2011; Byrnes et al., 2013; Liu et al., 2015; O'Donnell et al., 2017). Briefly, ATL protomers (presumably on trans membranes) bind GTP, while G domains are in an engaged state with middle domains (Byrnes and Sondermann, 2011; Bian et al., 2011; Byrnes et al., 2013; O'Donnell et al., 2017). Upon initiation of hydrolysis, G domains are released (O'Donnell et al., 2017) followed by dimerization in a crossover formation, bringing membranes in close proximity for fusion (Byrnes and Sondermann, 2011; Bian et al., 2011; Byrnes et al., 2013).

Despite our current understanding of the ATL catalytic cycle, questions remain about how this mechanism translates to efficient membrane fusion in the cell. Recent studies have shown that continuous GTP hydrolysis is required for efficient membrane tethering and fusion, that not all tethering events result in successful fusion (Liu et al., 2015; Saini et al., 2014), and that fusion efficiency increases cooperatively with increasing ATL surface density on the membrane (Liu et al., 2015). Yet it is not clear how efficient membrane fusion is achieved by individual GTP hydrolysis–dependent dimerization events. ATL protomers also appear to form a zipper-like ultrastructure at the interface of tethered proteoliposomes (Saini et al., 2014), hinting at a higher degree of assembly. Lastly, it is not known if there are mechanisms to reduce GTP hydrolysis and dimerization cycles between cis membrane protomers. Such cycles would be futile in membrane tethering and fusion and have been reported to occur between ATLs in vitro (Liu et al., 2015).

Here we present novel regulatory mechanisms that involve the short, understudied N-terminal motifs of vertebrate ATLs and that contribute to the efficiency and function of ATLs. Early studies identified these short motifs preceding the G domain, pointing out their conservation in sequence across homologues but divergence across isoforms (Zhu et al., 2003). We demonstrate that these hypervariable regions (HVRs) can adopt isoform-specific conformations, and in the case of ATL1, contribute to tethering efficiency. These motifs also contain some of the most reproducible phosphorylation sites found in unbiased screens for post-translational modifications in cellular proteomes (Hornbeck et al., 2015). We verify phosphorylation of ATL1's HVR on conserved serine residues, identify site-specific kinase candidates, and demonstrate a requirement of HVR phosphorylation for WT ATL1 function. Together, these studies indicate intrinsic and extrinsic modes of ATL regulation in vertebrates that rely on sequences outside the catalytic core and may contribute to the dynamic remodeling of ER membranes.

Results

ATL1 and ATL3 contain structured N-terminal HVRs

Previous crystal structures of human ATL isoforms reported the enzyme adopts multiple nucleotide-dependent conformations. These structures of ATL1 and ATL3 in combination with biochemical investigations revealed the basis for how GTP-hydrolysis orchestrates key events that result in membrane tethering and fusion (Byrnes and Sondermann, 2011; Bian et al., 2011; Byrnes et al., 2013; O'Donnell et al., 2017). In all preceding structures, the N-terminal residues leading from the initiator methionine to the G domain were largely disordered. The conservation of this region across different species is strong within distinct isoforms, but highly divergent when isoforms within a particular species are compared with each other (Fig. 1 A). Considering these characteristics, we refer to the N-terminal motif of ATLs as the HVR, in analogy to the C-terminal segments in small G proteins. Here, two structures are presented of ATL1 and ATL3, which reveal an ordered segment of secondary structure in this previously unresolved region (Table 1 and Fig. 1, B–D).

Datasets for native and selenomethionine-derivatized protein crystals grown from the GDP-bound catalytic core of hATL1 were collected at a resolution of 2.2 Å and 3.5 Å, respectively. Phases were experimentally calculated using the selenomethionine (SeMet) dataset and combined with the high-resolution reflections of the native dataset. Similar to other GDP-bound structures (Fig. S1 A), the G and middle domains are engaged in the prehydrolysis state, with an RMSD of 0.49 Å for ATL1 $R^{77}A$ and 0.56 Å for ATL1 WT (Protein Data Bank [PDB] accession nos. 6B9D and 3Q5E; Fig. 1 B; Byrnes and Sondermann, 2011; O'Donnell et al., 2018). At the N terminus, the HVR was partially resolved and consists of a short β-hairpin with strong electron density in an F_o-F_c omit map (residues 18–31, Fig. 1, B and D). The structure of the isolated ATL3 G domain was determined in the presence of GDP • Mg^{2+} at a resolution of 2.1 Å and solved by molecular replacement using the corresponding fragment of the ATL3 catalytic core (PDB accession no. 5VGR) as the search model (O'Donnell et al., 2017; Fig. S1 B). In contrast to ATL1, the HVR of ATL3 forms a single α-helix protruding from the G domain in one of the two ATL3 protomers in the asymmetric unit (residues 1–23 in Fig. 1, C and D).

Most strikingly, we determined that the HVR of ATL1 made direct contacts with the G domain of the adjacent protomer within the crystal lattice in a manner that, if extrapolated to predicted membrane orientations, would yield an array of HVR-dependent oligomers on a single membrane (Figs. 1 E and S1 A). Such an oriented oligomer could work to both coordinate the catalytic cycles of many ATLs and prime them for in trans interactions by presenting the G domain dimerization interface outwards toward the cytosol. The crystal lattice presents such an arrangement via the packing of the G domain (Fig. 1 E), which has been observed previously in GDP-bound structures of ATL1 (e.g., Byrnes and Sondermann, 2011; Bian et al., 2011; O'Donnell

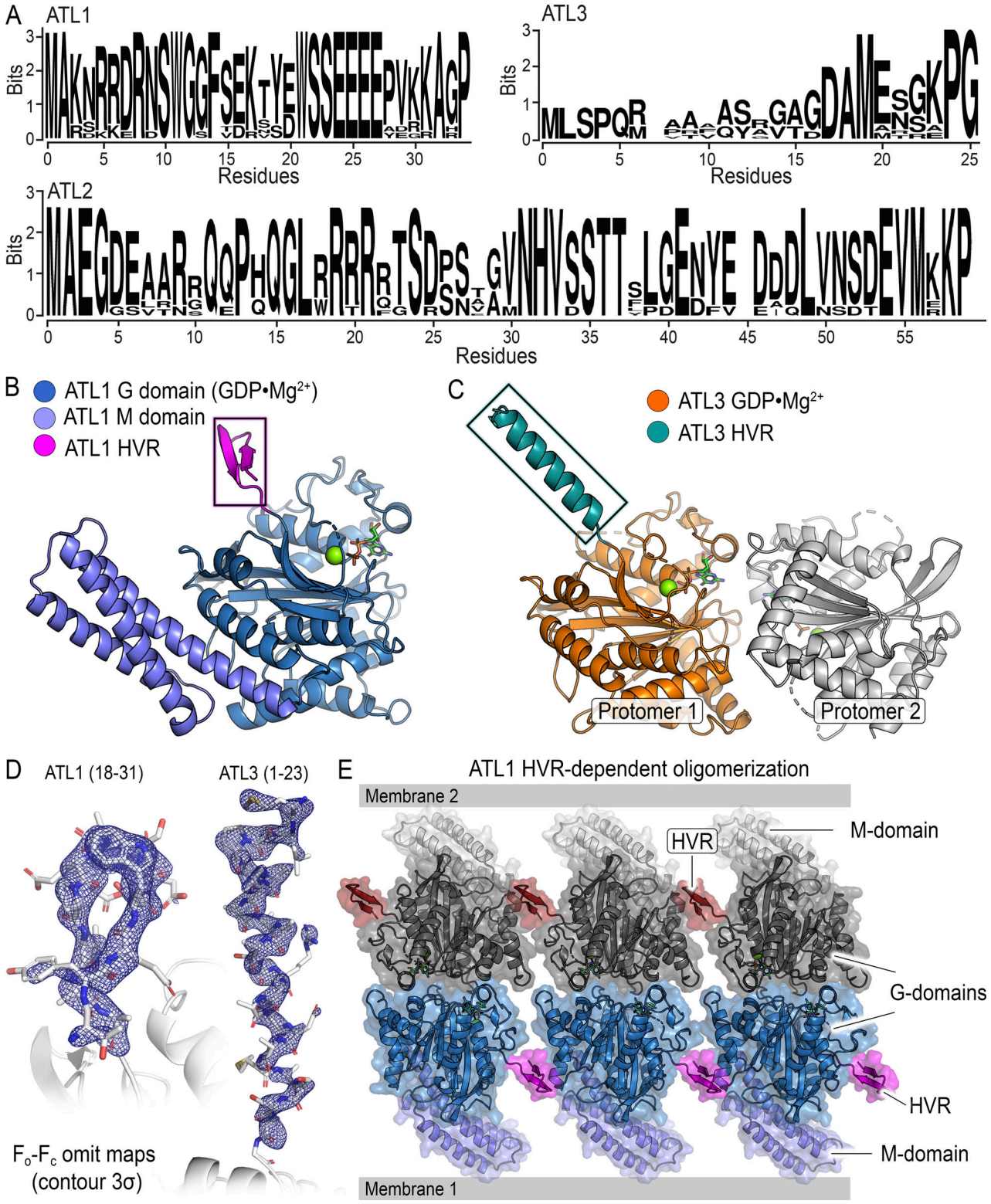

Figure 1. **ATL1 and ATL3 crystal structures resolve N-terminal motifs. (A)** Sequence logos of the HVR in ATL1 (1–33), ATL2 (1–59), and ATL3 (1–25) created using WebLogo (Crooks et al., 2004) from ATL sequences in human, dog, horse, rat, mouse, chicken, frog, zebrafish, and cow. **(B)** Structure of human ATL1 soluble domain (1–446) displayed in blue and the HVR (residues 18–31) in magenta. Ligands (GDP and Mg^{2+}) are shown with ball and stick representation. **(C)** Cartoon representation of human ATL3 G domain structure (1–334). Protomer 1 is shown colored orange with its HVR (1–25) in teal. GDP•Mg^{2+} is shown in ball and stick representation. Protomer 2 is shown in gray. **(D)** F_o-F_c maps show electron density of ATL1 (left) and ATL3 (right) HVRs from structures in B and C. Stick models for each structure are shown in gray and colored by element. Electron density maps are contoured at 3σ. **(E)** Organization of ATL1 structure with the HVR within the crystal lattice and extrapolated orientation of two opposing membranes (gray bars on top and bottom). Each protomer is represented in cartoon and surface view to display contacts.

Table 1. **X-ray data collection and refinement statistics**

	ATL1 1-439	**ATL1 1-439**	**ATL3 1-334**
	SeMet single anomalous diffraction	**Native refinement**	**Molecular replacement (PDB accession no. 5VGR)**
Data collection			
X-ray source	CHESS A1	CHESS A1	CHESS F1
X-ray wavelength (Å)	0.9767	0.9767	0. 9770
Space group	*I222*	*I222*	$P2_12_12_1$
Unit cell parameters			
a, b, c (Å)	54.0, 139.4, 200.6	54.2, 138.9, 202.2	44.5, 88.0, 168.8
α, β, γ (°)	90.0, 90.0, 90.0	90.0, 90.0, 90.0	90.0, 90.0, 90.0
Resolution range (Å)	50.00–3.50 (3.59–3.50)	45.16–2.20 (2.32–2.20)	50.00–2.10 (2.15–2.10)
No. of reflections			
Total	165,958 (12,547)	350,545 (51,572)	317,439 (23,823)
Unique	18,450 (1,375)	39,278 (5,640)	39,632 (2,864)
Completeness (%)	99.9 (100.0)	100.0 (100.0)	99.9 (100.0)
Multiplicity	9.0 (9.1)	8.9 (9.1)	8.0 (8.3)
I/σ(I)	12.6 (11.8)	16.2 (3.2)	14.7 (1.5)
R_{meas} (%)	34.8 (36.1)	7.8 (73.5)	10.5 (151.7)
$CC_{1/2}$ (%)	97.2 (96.9)	99.8 (90.2)	99.9 (66.5)
Anomalous correlation (%)	43 (18)	-	-
Refinement			
R_{work} / R_{free} (%)	-	20.1 / 23.7	17.9 / 23.1
RMS deviations			
Bond length (Å)	-	0.007	0.008
Bond angle (°)	-	0.905	0.913
No. of atoms			
Protein	-	3283	4785
Ligands	-	29	58
Water	-	85	240
Average B-factors (Å^2)			
Total	-	67.2	53.0
Protein	-	67.4	53.4
Ligands	-	65.5	34.8
Waters		60.3	49.6
Ramachandran (%)			
Favored	-	95.6	97.5
Outliers	-	0.0	0.0
PDB accession no.	-	6XJN	6XJO

Values in parentheses represent the highest resolution bin.

et al., 2018). The interface surface area between the HVR and G domain of ATL1 is 312 Å^2 and provides a favorable solvation free energy gain (Δ^iG) of −6.2 kcal/mol (Krissinel and Henrick, 2007). The α-helical HVR of ATL3 also makes a crystal contact with a G domain from a neighboring unit cell, though it exhibits a different mode of interaction when compared with ATL1 (Fig. S1). As the ATL3 structure is comprised of the isolated G domain, the mechanistic implication of this interaction remains to be investigated.

HVR deletion does not affect nucleotide-dependent dimerization or GTPase activity

The HVR is not expected to contribute to oligomerization or catalytic rates of soluble ATL protein fragments, considering the

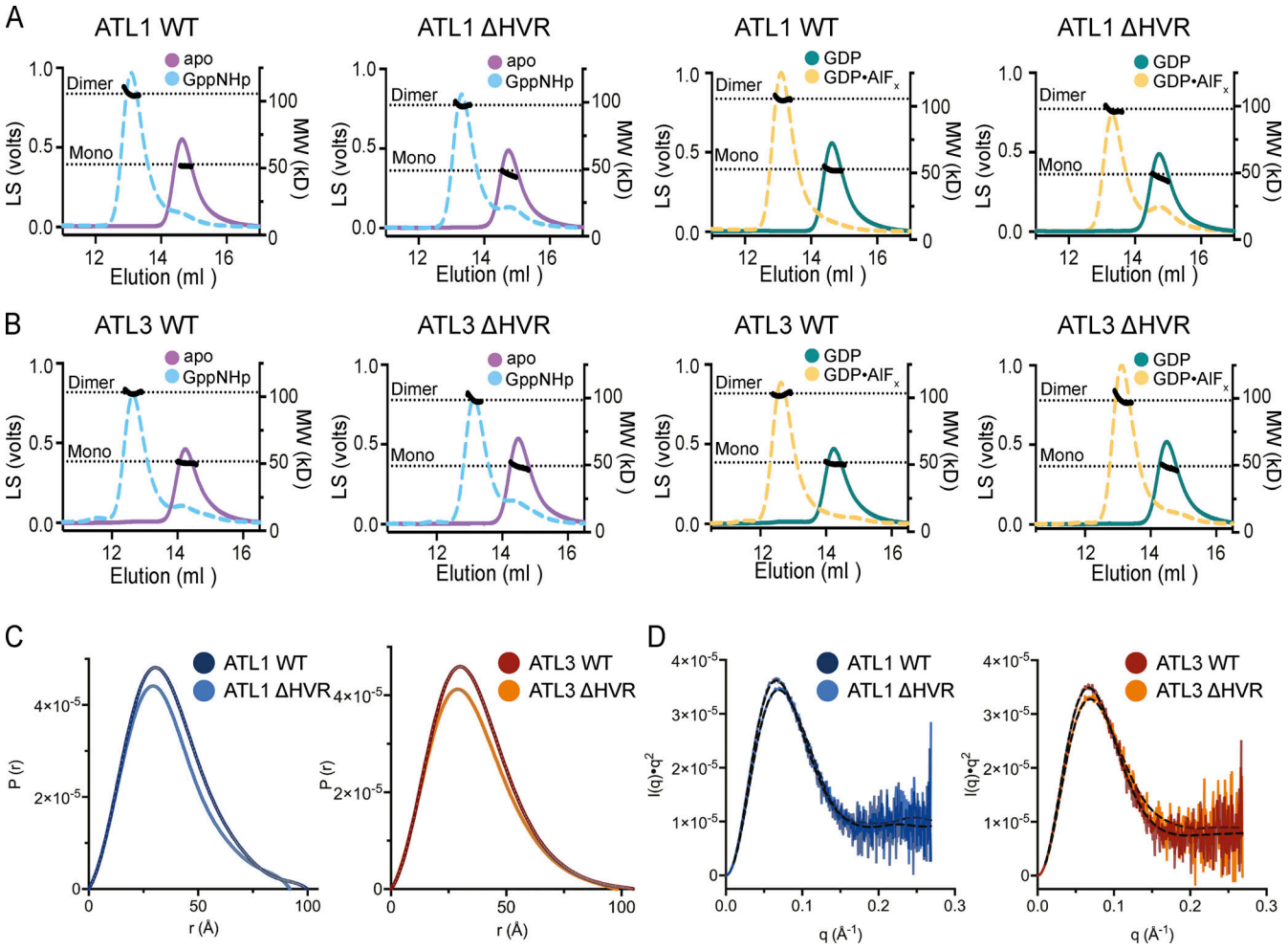

Figure 2. **Removal of the HVR maintains nucleotide-dependent oligomerization of ATL1 and ATL3 in solution. (A)** Molecular weight (MW) determination with SEC-MALS was used to monitor oligomerization of catalytic core of WT (left) and ΔHVR (right) ATL1^{10xHIS} in several nucleotide-bound conditions: apo (no ligand bound; purple), guanosine 5′-[β,γ-imido]triphosphate (GppNHp; blue), GDP (teal), or GDP•AlF^{4-} (yellow). The left y axis shows light scattering signal (LS) in volts as colored lines, the right y axis shows calculated molecular weights in kilodaltons (kD) as black lines across elution peaks (with dashed lines at theoretical dimer/monomer weights, indicated as "dimer" or "mono" on the graph), and the x axis is the elution volume in milliliters (ml). **(B)** ATL3 WT and ΔHVR were used in the same experimental set-up as in A. **(C)** Small-angle x-ray scattering was performed on the catalytic core of ATL1 and ATL3 with and without their respective HVRs in the presence of 2 mM GDP. Plotted here is the pairwise distance distribution, with the relative P(r) scale on the y axis and real-space distances (r(Å)) on the x axis in Å. **(D)** Kratky plots for each condition in C with experimental data represented in the corresponding colors and theoretical data shown by the dotted black lines. The y axis plots I(q)·q^2, where q is the scattering angle and I(q) is signal intensity as a function of q. The scattering angle (q) is plotted on thex axis in units of Å^{-1}.

lack of evidence for higher-order interaction in solution and as based on the structural analysis suggesting a rather weak interaction. To formally assess the effect of the HVR on ATL's oligomerization in solution, we conducted size-exclusion chromatography (SEC) coupled to multi-angle light scattering (MALS) in several nucleotide-bound conditions for ATL1 and ATL3 with and without HVRs (Fig. 2, A and B). Calculated molecular weights confirmed that the oligomerization states were not affected by deletion of the HVR and agree with dimerization trends reported previously (Byrnes and Sondermann, 2011; O'Donnell et al., 2017). Additionally, small-angle x-ray scattering (SAXS) experiments were conducted with the same WT and ΔHVR proteins in the presence of GDP and Mg^{2+} (Table 2). Both the pairwise distance distributions (Fig. 2 C) and the Kratky plots (Fig. 2 D) show negligible deviations for either ATL1 or ATL3 with the deletion of the HVR, which indicates that the conformation and folded state of the proteins are equivalent.

Similarly, we hypothesized the HVR would not affect GTPase rates. We tested the effect of the HVR on ATL's GTPase activity in solution by determining phosphate release kinetics using ATL catalytic cores (i.e., constructs with G and middle domains) with or without deletion of the HVR. Phosphate release rates were determined at various protein concentrations, and the turnover numbers (k_{cat}) for WT and ΔHVR proteins were nearly identical for corresponding isoforms (Fig. 3 A). Together and as predicted, the data confirm that the HVR deletion in ATLs does not influence the solution characteristics of the protein's catalytic core.

Table 2. **Small-angle x-ray scattering statistics**

	Guinier		GNOM P(r)		
	qRg	Rg	Quality estimate	Rg (Å)	Dmax (Å)
ATL1 WT	0.32–1.29	28.55 ± 0.065	82.49	28.92 ± 0.074	100
ATL1 ΔHVR	0.28–1.18	27.75 ± 0.071	80.41	28.13 ± 0.053	92
ATL3 WT	0.28–1.30	27.68 ± 0.071	85.62	28.32 ± 0.11	106
ATL3 ΔHVR	0.28–1.29	27.20 ± 0.090	85.77	27.75 ± 0.077	94

Deletion of the HVR compromises membrane tethering kinetics in ATL1 but not ATL3

Based on the structural model, we posit that the HVR may be involved in higher-order oligomerization of ATLs but exudes functionality only when ATLs are restricted to a two-dimensional membrane where weak interactions can become more robust due to increased protein concentrations (Kuriyan and Eisenberg, 2007). To test whether the HVR plays a functional role in membrane-related ATL function, which we may assume based on our model, we assessed the ability of ATLs to tether membranes, a crucial step in the fusion process (Fig. 3, B–E). The catalytic core proteins were expressed with a C-terminal decahistidine tag that enables association with the surface of membrane vesicles containing Ni^{2+}-nitrilotriacetic acid (Ni^{2+}-NTA)–modified lipids (at a 1% molar ratio). The protein's orientation on the vesicle surface is conducive for trans dimerization akin to the full-length transmembrane protein on the surface of the ER (Liu et al., 2015). Upon the addition of GTP, ATL catalyzes the tethering of vesicles, resulting in formation of vesicle clusters that increase the solution's turbidity, which can be measured by light scattering at 360 nm. The experiment was performed across increasing protein concentrations while keeping lipid concentrations constant.

For ATL1 WT, the rate of tethering exhibited a strong dependency on protein concentration, and this dependency was abolished with the deletion of the HVR, although basal tethering was detectable consistent with basic, GTPase-dependent dimerization of the ATL1 ΔHVR (Fig. 2 A; and Fig. 3, B and D). Tethering rates were substantially slower in WT ATL3, and neither WT nor ΔHVR displayed concentration-dependent tethering kinetics (Fig. 3, C and D). To rule out differences in apparent tethering rates were caused by reduced lipid loading efficiency of the ΔHVR construct, we subjected WT ATL1 and ΔHVR to density gradient centrifugation in the presence and absence of lipids (Liu et al., 2015) and analyzed gradient fractions (Fig. S2 A). The SDS-PAGE analysis confirmed that deletion of ATL1's HVR did not impact lipid binding of the proteins used in these assays. Additional tethering controls were performed (Fig. S2 B), including addition of 100 mM EDTA or 500 mM imidazole after 45 min, resulting in elution of protein from lipid vesicles and a subsequent drop in OD_{360} signal. Reactions were also performed in the absence of $MgCl_2$ or with GDP instead of GTP. These controls confirmed that tethering required ATL proteins on the surface of liposomes as well as GTP hydrolysis.

Observed tethering rate constants as a function of protein concentration indicate a robust tethering enhancement of WT ATL1 with a strong dependence on the HVR (Fig. 3, B and D). At later time points, WT ATL1 samples produced macroscopic, tethered clusters that were visually discernable and occurred when tether formation began to plateau, causing high signal variation (Fig. 3, B and E). Tethered clusters cleared from solution upon elution of ATL from vesicles as shown in Fig. S2. Macroscopic tethering and signal variation did not occur at later time points in ATL3 (Fig. 3 C).

ATL1's HVR is phosphorylated on three conserved serine residues

The HVR of ATL1 was predicted to be post-translationally modified, and given the strong HVR-dependent phenotype in membrane tethering, we speculated that HVR modification in ATL1 may provide a mode of regulation in vivo. Unbiased proteomic screens predict modifications at 11 locations, with the most reproducible modifications being phosphorylation within the HVR at S^{10}, S^{22}, and S^{23} (PhosphoSitePlus v.6.5.9.3; Hornbeck et al., 2015; Fig. 4 A).

We experimentally confirmed the predictions by monitoring the phosphorylation status of exogenously expressed ATL1 in U2OS cells, a human osteosarcoma cell line. Cell lysates were analyzed by immunoblotting both denaturing SDS-PAGE and Phos-tag gels against a C-terminal Myc epitope on the recombinant proteins (Fig. 4 B; Kinoshita et al., 2009). The Phos-tag reagent interacts specifically with phosphorylated species, affecting their electrophoretic mobility. The WT sample exhibited two higher-order populations in the Phos-tag immunoblot (indicated in Fig. 4 B as "1" and "2"), which collapsed to a single species in the immunoblot from denaturing SDS-PAGE without Phos-tag reagent. Upon deletion of the ATL1 HVR, both Phos-tag and standard denaturing SDS-PAGE immunoblots depicted single populations (Fig. 4 B). These data confirm that WT ATL1 is phosphorylated on the HVR at one or more positions in cells.

To gain residue-specific resolution of the phosphorylation events on ATL1, we used liquid chromatography with tandem mass spectrometry (LC-MS/MS). Exogenously expressed WT ATL1 was immunoprecipitated from U2OS cell lysate, trypsin-digested, and subjected to LC-MS/MS. We observed phosphorylation on the three highest confidence residues listed in the PhosphoSitePlus database: S^{10}, S^{22}, and S^{23} (Fig. 4 C). Shown are the two phosphorylated peptides identified by mass spectroscopy: peptide 1 (green) included S^{10}, which was only observed in its phosphorylated state; and peptide 2 (maroon) included S^{22} and S^{23}, which were found to be present in one of two states, both phosphorylated or neither phosphorylated. The fraction of

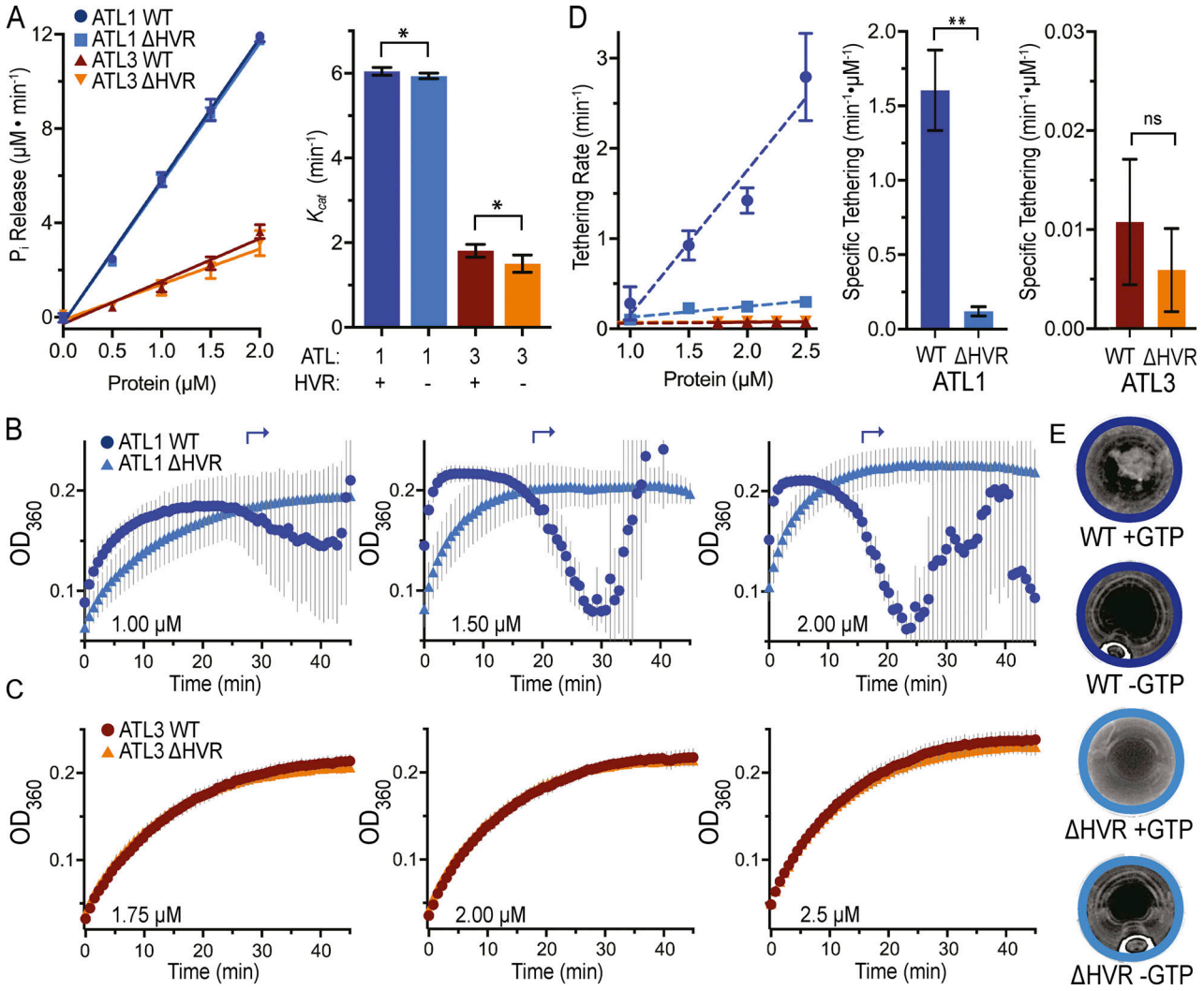

Figure 3. **The HVR contributes to ATL1-mediated membrane tethering. (A)** Phosphate release kinetics (left) across increasing protein concentrations and k_{cat} values (right) for the catalytic core of ATL1 and ATL3 WT and ΔHVR. All kinetic experiments were performed with two biological and three technical replicates (n = 6), with error bars showing SD (where not visible, errors were smaller than symbols representing means). ATL1 WT and ΔHVR are 6.05 ± 0.039 min^{-1} and 5.94 ± 0.028 min^{-1}, respectively, with P = 0.049; ATL3 WT and ΔHVR are 1.81 ± 0.062 min^{-1} and 1.51 ± 0.084 min^{-1}, respectively, with P = 0.015. Statistical significance was determined by unpaired, two-tailed t test, assuming Gaussian distribution of data. Here and in all figures, statistical significance is denoted as: ns, P > 0.05; *, P ≤ 0.05; **, P ≤ 0.01; ***, P ≤ 0.001; and ****, P ≤ 0.0001. **(B)** Tethering reactions of $ATL1^{10xHIS}$ WT (dark blue) and ΔHVR (light blue) at increasing protein concentrations and fixed lipid (1 mM) and GTP (500 μM) concentrations. A rise in OD_{360} signal over time indicates increasing turbidity of the solution due to an increase in vesicle cluster number or size. Erratic signal and/or signal drops at later time points correlate with the appearance of macroscopic clusters that are visible with the naked eye (marked by dark blue arrows). All tethering reactions were performed with two biological and three technical replicates. The mean signal at OD_{360} is shown with the SD in gray across the 45-min reaction. **(C)** As in B but with $ATL3^{10xHIS}$ WT (maroon) and ΔHVR (orange). **(D)** Left: Tethering rates (min^{-1}) were plotted for each construct at increasing concentrations with linear regressions shown for each, and error bars showing SD. Right: Specific tethering (min^{-1}•μM^{-1}) was calculated for each protein construct on the left, and statistical significance was determined with an unpaired, two-tailed t test (ATL1 WT and ΔHVR P = 0.0055; ATL3 WT and ΔHVR P = 0.5642). Distribution of the data was assumed to be normal. **(E)** Photographic images (top view of the reaction well) of $ATL1^{10xHIS}$ ± HVR tethering reactions after 45 min with and without GTP.

total peptides with the phosphorylated residues is shown in Fig. 4 D, with pS^{10} observed on 100% of S^{10} and pS^{22}/pS^{23} occurring on 24% of observed $S^{22/23}$-containing peptides. As shown in Fig. 4 E, these three serine residues are strictly conserved within ATL1's HVR.

The $S^{10}E$ phosphomimetic mutant decreases ATL1 tethering rates but not catalytic activity

Having verified that ATL1 was phosphorylated in vivo, we were interested in establishing if these modifications would impact catalytic activity. This was achieved by comparing WT protein to proteins with serine-to-glutamate mutations at sites of phosphorylation, which mimic the charge density of phosphorylated serine residues. The k_{cat} values for each protein were similar between WT and those of proteins with phosphomimetic mutations at sites that we confirmed to be modified in cells ($S^{10}E$ and $S^{22}E/S^{23}E$): WT: 6.05 ± 0.04 min^{-1}, $S^{10}E$: 5.97 ± 0.40 min^{-1}, and $S^{22}E/S^{23}E$: 6.31 ± 0.55 min^{-1} (Fig. 5 A). Since we observed that S^{10} was entirely phosphorylated in cells, this modification must coexist with phosphorylation of S^{22}/S^{23}. Therefore, the

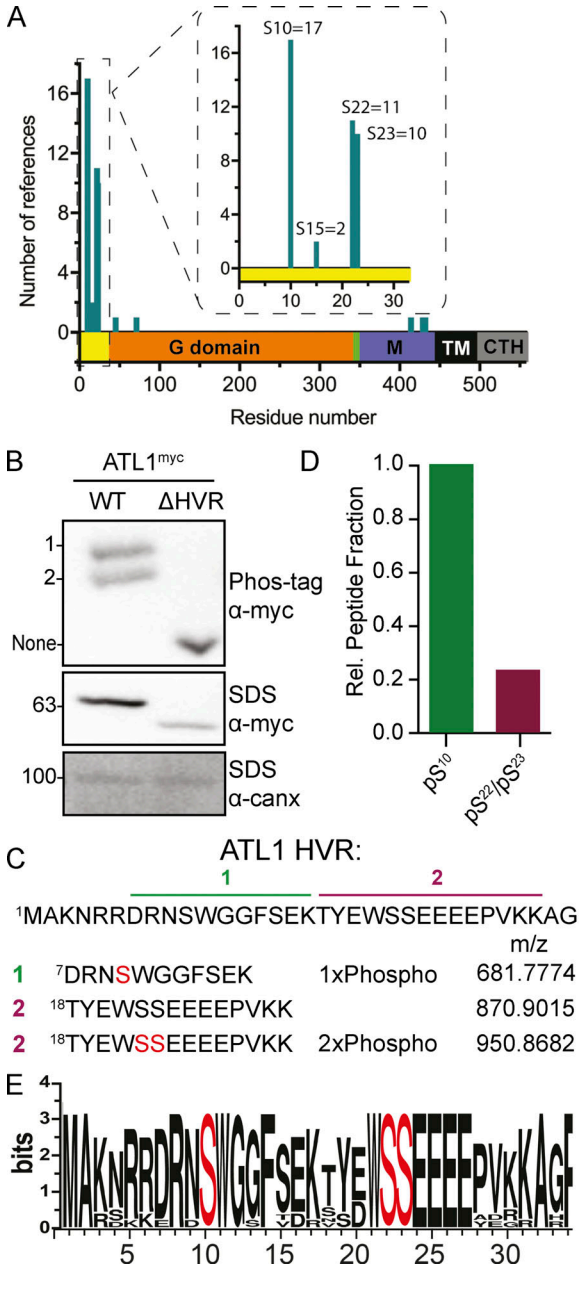

Figure 4. **Several serine residues in ATL1's HVR are phosphorylated.** **(A)** Reported phosphorylation of individual residues within human ATL1, compiled by PhosphoSitePlus v.6.5.9.3 (Hornbeck et al., 2015) with teal bars showing number of reports from unbiased proteomics screens citing a phosphorylation. The x axis color codes residue number by structural domain (yellow = HVR, orange = G domain, green = flexible linker, purple = middle (M) domain, black = transmembrane (TM) domain, and grey = C-terminal helix [CTH]). The inset of the graph magnifies the HVR and labels total reference numbers for each Ser in the database. **(B)** Western blots of U2OS lysates transfected with ATL1^{myc} ± its HVR. Blots of a Phos-tag gel (top) and SDS-PAGE (middle) are shown, both probed with α-c-myc. The bottom blot from an SDS-PAGE was probed with α-calnexin as a loading control. Total protein in lysate was quantified and normalized before gel loading. Molecular weights indicated as kilodaltons on the left (SDS-PAGE only). Standards were omitted from Phos-tag gels since their separation relies on both molecular weight and phosphorylation state of the analyte, causing aberrant migration of proteins and molecular weight markers. **(C)** LC-MS/MS of WT ATL1^{myc} identified two peptides within the HVR with variably phosphorylated serine residues (peptide 1, green, S^{10}-containing; peptide 2, maroon, S^{22}/S^{23}-containing). The number of modifications is indicated as well as m/z (mass-to-charge ratio, m = atomic mass and z = formal charge) for each peptide. **(D)** Graph indicating the relative peptide fraction containing the phosphorylated species for peptides 1 and 2, respectively. **(E)** WebLogo of ATL1 HVR with its three phosphorylated serine residues identified in mass spectroscopy shown in red.

$S^{10}E/S^{22}E/S^{23}E$ triple mutant was tested and showed a minor decrease in P_i release to 5.41 ± 0.15 min^{-1}.

Similar to experiments described for the HVR-deletion mutant, we used a vesicle tethering assay to elucidate how ATL1 phosphorylation may regulate function at the membrane. Protein concentration–dependent tethering assays were conducted with WT and phosphomimetic mutations that correspond to in vivo phosphorylation states. Fig. 5, B and C, shows that the variant with a glutamate substitution at the most prevalent phosphorylation site, $S^{10}E$, displayed a strong reduction in the rates of tethering. A corresponding mutant mimicking the less abundant pS^{22}/pS^{23} modifications was not statistically different from WT. Combination of all phosphomimetic positions resulted in in a tethering phenotype comparable to that of $S^{10}E$ alone, indicating that modification of S^{10} is the major contributor to decreased tethering kinetics. The effect of the $S^{10}E/S^{22}E/S^{23}E$ mutant was noticeable also upon inspections of the reaction wells, with the mutant not showing the macroscopic vesicle aggregates that were observed with the WT protein.

Catalytic activity and vesicle tethering experiments were conducted with serine-to-alanine mutations in the same combinations used to mimic phosphorylation to ensure mutations were specific to the characteristics of the side chain rather than general effects of altering the sequence. In all cases, ATL1 proteins with alanine substitutions in S^{10}, S^{22}, and S^{23} reflected the catalytic and tethering rates of WT ATL1 (Fig. S3).

ATL1 HVR phosphomimetic mutants alter protein localization at the ER

We established that incorporating phosphomimetic mutations at sites of endogenous phosphorylation modulates ATL function in vitro. This effect was exclusive to measurements made while ATLs were associated with membranes. To investigate how phosphorylation may regulate ATL function at the ER, we conducted immunofluorescence imaging of cells expressing either serine-to-glutamate or serine-to-alanine mutations that mimic the phosphorylated and dephosphorylated states, respectively.

To exclusively measure the effects of phosphomimetic mutations, we used a NIH-3T3 cell line, in which all three ATL isoforms were deleted using CRISPR/Cas9-mediated gene editing (Zhao et al., 2016). Upon addback of WT ATL1 to the triple knockout (TKO) cell line, ER morphology reverted to the same as in the parent NIH-3T3 cell line (Fig. 6 A), showing a branched ER network in lieu of long, unbranched ER tubules reported for the TKO cell line. The S^{10}, S^{22}/S^{23}, $S^{10}/S^{22}/S^{23}$ phosphorylation site iterations were tested with both glutamate and alanine mutations. All ATL1 phosphomimetic mutants were shown to correctly localize to the ER by imaging cotransfected cells with an mCherry-tagged ER resident membrane protein, Sec61β (Fig. S4; Zurek et al., 2011). In the following, we mainly refer to ATL1 ER

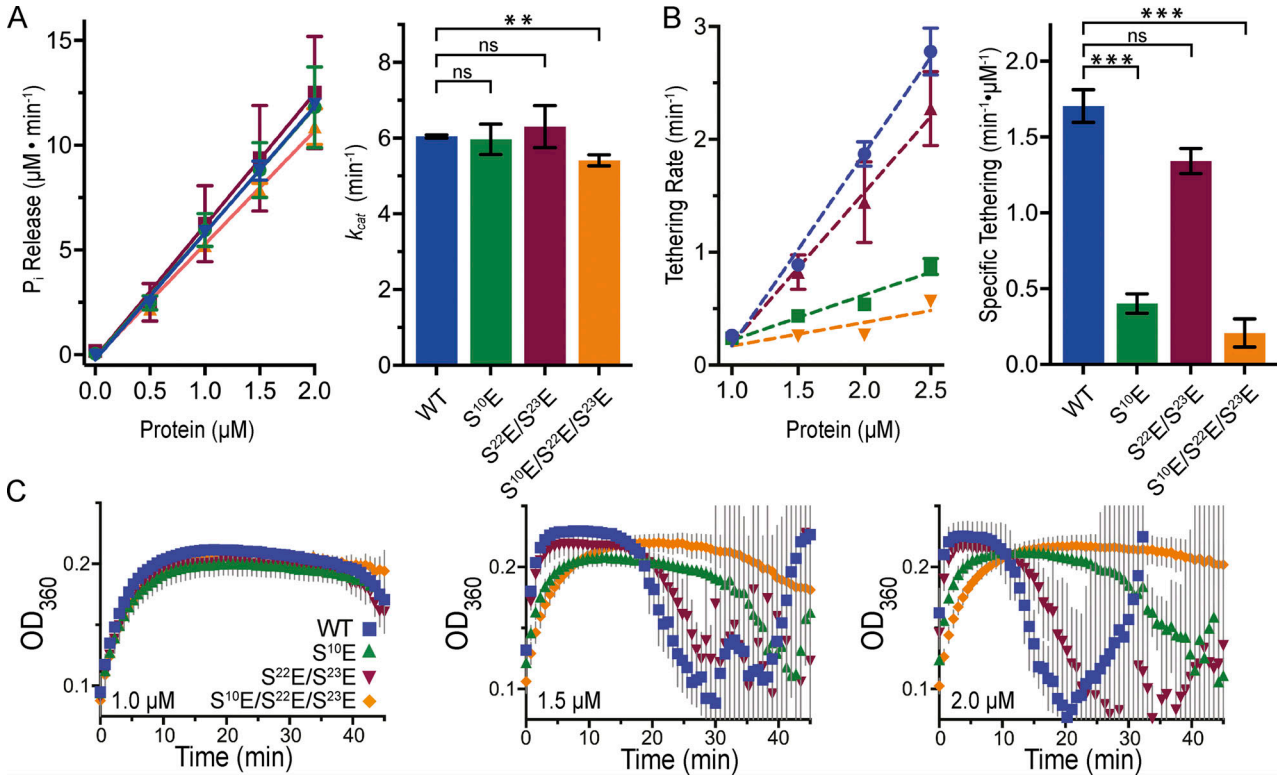

Figure 5. **Phosphomimetic ATL1 variants show altered vesicle tethering kinetics without affecting GTPase rates. (A)** Left: Phosphate release kinetics of ATL1 WT (blue), S^{10}E (green), S^{22}E/S^{23}E (maroon), and S^{10}E/S^{22}E/S^{23}E (orange) across protein concentrations of 0 to 2 μM. Each data point is the average μM P$_i$/min released across three technical and two biological replicates (n = 6) with error bars showing SD. Right: k_{cat} for each mutant. Statistical significance was calculated using an unpaired, two-tailed t test against ATL1 WT (ATL1 S^{10}E P = 0.8567; S^{22}E/S^{23}E P = 0.6498; and S^{10}E/S^{22}E/S^{23}E P = 0.0019), with the assumption of normal data distribution. **(B)** Left: Initial tethering rate (min^{-1}) for each mutant at each protein concentration. The slope for each mutant construct was calculated and values plotted in the graph on the right with statistical significance tested as in A compared with WT protein (P = 0.0005 for ATL1 S^{10}E; P = 0.0557 for ATL1 S^{22}E/S^{23}E; P = 0.005 for ATL1 S^{10}E/S^{22}E/S^{23}E). **(C)** Vesicle tethering reactions of ATL1 WT and phosphomimetic mutants at increasing protein concentrations (indicated) and constant lipid concentration (1 mM). Replicate type and number as described in Fig. 3, B and C.

distribution when ATL1 expression is probed. However, since ATL1 WT and variants associate with the ER membrane, their localization likely correlates with overall ER morphology, except for punctate ATL1 localization, which appears to mark specific junction sites within the ER (Nixon-Abell et al., 2016).

Addback experiments resulted in changes to ATL localization. ATLs were found at two major ER locations, ER tubes (WT phenotype) and ER puncta. Based on the ATL1 staining, two global ER morphologies are also reported, the reticular structure (WT phenotype) and a largely diffuse structure, which adopted a "fuzzy" appearance. The aforementioned localizations and morphologies were found across all exogenously expressed ATL constructs and were subsequently quantified (Fig. 6, B–F). All mutation iterations of the phosphorylation sites resulted in a subtle reduction in the number of cells having discernable ER tubules, except for the protein with glutamate substitutions at S^{22}/S^{23} (Figs. 5 E and 6 C). The phosphorylation mimetic at S^{22}/S^{23} resulted in a more substantial reduction in cells with discernable ER tubules (~40%), while the corresponding alanine mutation had no such effect. It is noteworthy that combining the glutamate mutation at S^{22}/S^{23} with S^{10}E resulted in a rescue of tubules, indicating that normal phosphorylation and/or turnover at site S^{10} exhibits dominance over the phenotype (Fig. 6, D and E). In contrast, all mutants expressed resulted in their accumulation in puncta at the ER, with position S^{10} contributing the most to this phenotype as seen in the variants with S^{10} modified alone and in combination with S^{22}/S^{23} (Fig. 6 E). Additionally, the alanine mutation of S^{10} caused more cells with puncta staining than the corresponding glutamate mutation (Fig. 6, B and E). The prevalence of cells with discernable ER tubes and puncta were observed to varying degrees for both S^{10}E and S^{10}A variants, which indicates that regulation may require cycling between phosphorylated and dephosphorylated states. At least, it suggests that for WT function, the unphosphorylated ATL1 is required as well as the phosphorylated species.

We also observed variable shifts in ATL's reticular localization pattern to a diffuse, fuzzy appearance depending on the phosphomimetic combination expressed. While the S^{10} glutamate and alanine mutants did not display this shift, expression of the S^{22}/S^{23} glutamate mutant resulted in nearly all cells containing a fuzzy ATL localization (Fig. 6, B, C, and F). Strikingly, expression of the S^{22}/S^{23} alanine mutant remained reticular comparable to WT ATL1. The physiological relevance of this result is unclear since phosphorylation of S^{22}/S^{23} appears unlikely to exist in the absence of S^{10} phosphorylation, which, when combined, lessens the morphology's prevalence (Fig. 6, D and F).

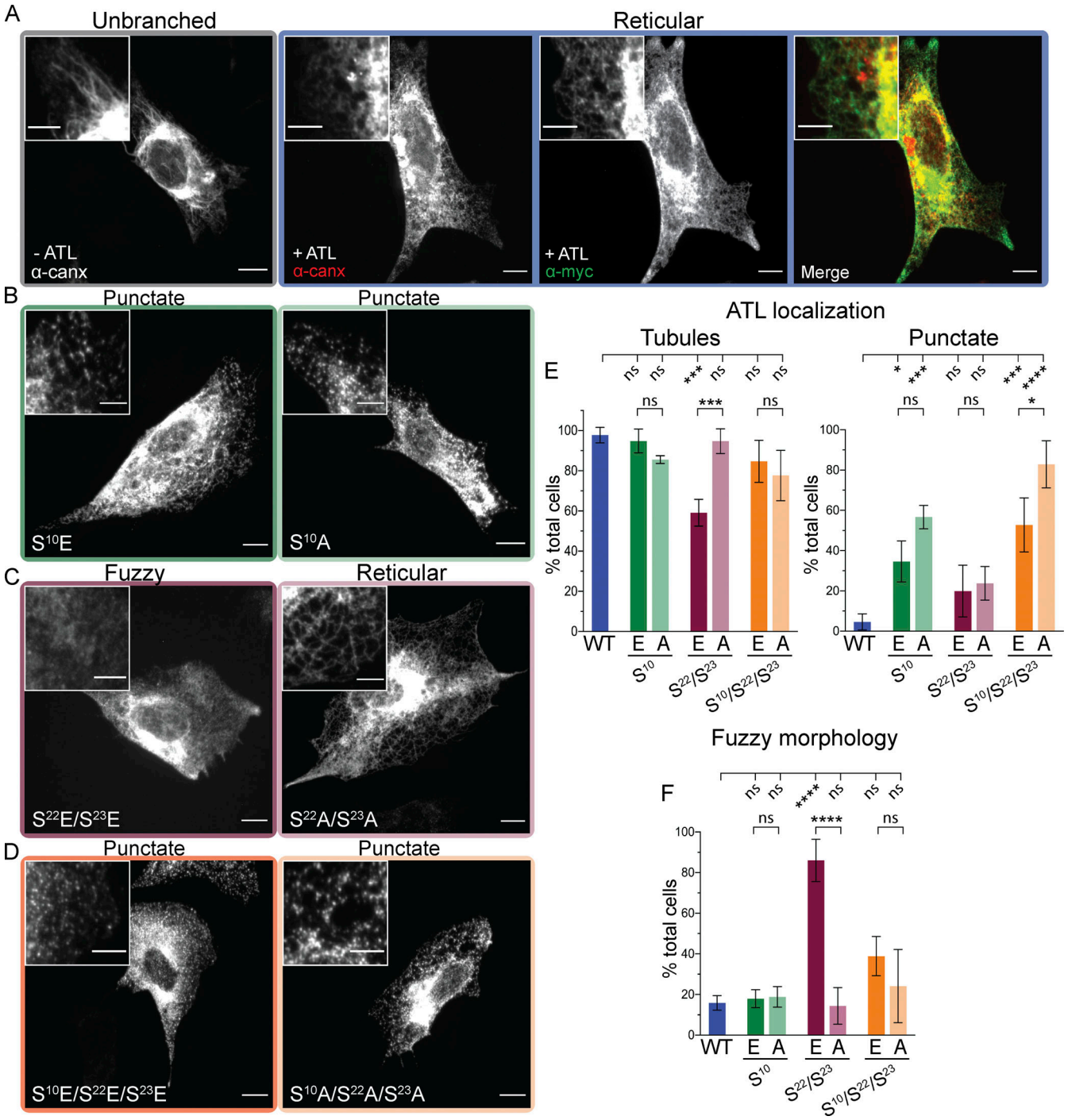

Figure 6. **HVR phosphomimetic mutations alter ATL1 ER distribution in mammalian cells. (A)** NIH-3T3 ALT1/2/3 TKO cell imaged by immunofluorescence against endogenous ER-resident protein calnexin (canx; gray box). The same cell type exogenously expressing c-myc–tagged WT ATL1 and imaged by immunofluorescence against endogenous calnexin (left) and c-myc (middle). Merged signals on the right (blue box). Main image scale bar = 10 µm; inset image scale bar = 5 µm. **(B–D)** Representative images of NIH 3T3 ATL1/2/3 TKO cells transiently transfected with c-myc–tagged, phosphomimetic mutant ATL1 constructs, probed against c-myc: (B) $S^{10}E$ (green) or $S^{10}A$ (light green); (C) $S^{22}E/S^{23}E$ (maroon) or $S^{22}A/S^{23}A$ (pink); and (D) $S^{10}E/S^{22}E/S^{23}E$ (orange) or $S^{10}A/S^{22}A/S^{23}A$ (light orange). Each image is labeled with the most prominent phenotype observed for that condition. **(E)** Percentage of cells in A–D with tubule (left) and punctate (right) ATL localization. For each sample, a minimum of 70 cells was imaged (or 44 for ATL1 WT). The mean of three experiments is represented with SD represented by error bars. Statistical significance was determined by one-way ANOVA. The data were assumed to have normal distribution. Here and in all figures, statistical significance is denoted as: ns, $P > 0.05$; *, $P \le 0.05$; **, $P \le 0.01$; ***, $P \le 0.001$; and ****, $P \le 0.0001$. **(F)** Quantification of cells in each condition with a fuzzy morphology of ATL signal. Represented as in E.

A

Mutant	Peptide	Phospho-Ser	m/z
$S^{22}A/S^{23}A$	1-[7]DRNSWGGFSEK	1	681.777
$S^{10}A$	2-[18]TYEWSSEEEEPVKK	None	870.901
	2-[18]TYEWSSEEEEPVKK	1	910.885
	2-[18]TYEWSSEEEEPVKK	1	910.885
	2-[18]TYEWSSEEEEPVKK	2	950.868
$S^{10}A/S^{22}A/S^{23}A$	1-[7]DRNAWGGFSEK	None	633.797
	2-[18]TYEWAAEEEEPVKK	None	854.909

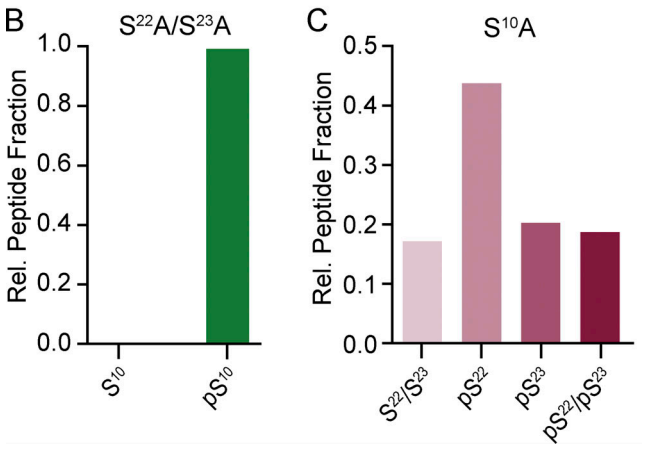

Figure 7. **Hierarchical order of ATL1 HVR phosphorylation. (A)** Peptides identified in LC-MS/MS analysis of ATL1 mutant proteins indicated. Phosphorylated serine residues are shown in red, the number of phosphorylated residues is specified for each peptide, and m/z (mass-to-charge ratio, m = atomic mass and z = formal charge) is shown for each identified peptide. **(B)** Relative peptide fraction identified in LC-MS/MS analysis of ATL1 $S^{22}A/S^{23}A$ for the phosphorylated peptide 1 (from A). **(C)** As in B, but for the variably phosphorylated peptide 2 from LC-MS/MS analysis of ATL1 $S^{10}A$.

Hierarchical order of ATL1 HVR phosphorylation

Biochemical and cellular experiments resulted in varying phenotypes depending on which phosphorylation site was investigated. In addition, the abundance of phosphorylation at a given site varies as determined by mass spectroscopy. These observations led us to posit that phosphorylation of S^{10}, S^{22}, and S^{23} may be dependent on each other and occur hierarchically. To test this, we investigated the phosphorylation state of the aforementioned serine-to-alanine point mutants. Lysates from U2OS cells expressing each mutant were investigated using LC-MS/MS, and the peptides of interest and their corresponding mass-to-charge ratios are reported (Fig. 7 A). We first evaluated the $S^{22}A/S^{23}A$ mutant to determine if S^{10} could be phosphorylated. Similar to the mass spectrometry experiment with WT ATL1 (Fig. 4), all identified peptides containing S^{10} in the ATL1 $S^{22}A/S^{23}A$ sample were found to be phosphorylated (Fig. 7 B). This indicates phosphorylation at position S^{10} occurs independently of S^{22} or S^{23} modification. In contrast, the ATL1 $S^{10}A$ sample displays a variety of phosphorylation states on residues S^{22} and S^{23} that were not represented in the WT sample (Fig. 7 C). In the WT ATL1 sample, S^{22} and S^{23} were always modified together; pS^{22} or pS^{23} did not exist independently. In the ATL1 $S^{10}A$ sample, 17.2% of the relative peptide fraction was fully un-modified, 18.8% was phosphorylated at both S^{22} and S^{23}, 43.8% was singly phosphorylated on residue S^{22}, and 20.3% was singly phosphorylated on S^{23}. The differences in phosphorylation patterns observed on residues S^{22} and S^{23} in the absence of pS^{10} imply a coordination of these modifications relying on an intact S^{10} site for phosphorylation. It remains unclear what the impact of such a regulatory mechanism may be, as S^{10} appears to be phosphorylated nearly, if not entirely, constitutively. However, as previously noted, the fact that we see significant ER morphological disruptions in both glutamate and alanine mutants at position 10 would indicate that there should be a transition from unphosphorylated to phosphorylated or turnover of this modification, the extent and kinetics of which are not yet understood.

Identification of putative kinases modifying conserved serine residues in ATL1's HVR

Due to hierarchical (or coordinated) phosphorylation of the HVR, we hypothesized that one or more specific kinase(s) may recognize ATL1. Determining the kinase candidates would be a first step in uncovering ATL regulation and the cellular pathways involved. To identify kinases that specifically phosphorylate ATL1, we screened a library containing 58 Ser/Thr kinase domains (Albanese et al., 2018). Small-scale reactions were conducted for each kinase, with and without ATP and the recombinant ATL1 catalytic core that historically includes the entire HVR. Reactions were analyzed by denaturing SDS-PAGE, and the acrylamide gels were stained with ProQ Diamond phosphoprotein stain, which selectively stains phosphoproteins; the fluorescent signal was quantified using ImageJ (Schneider et al., 2012). The ratio of ProQ stain signal between reactions with and without ATP represents the fold-increase of phosphorylation over background (Fig. 8 A). To exclude the possibility of signal attributed to auto-phosphorylation of the kinase, reactions without ATP and/or ATL1 were conducted for each kinase (Fig. S5). The screen identified several kinase families to be strong modifiers of ATL1 in vitro, which include casein kinase II (CK2 α and α' catalytic subunits), p21-activated kinases (PAK7/5, PAK 6, and PAK4), Ca^{2+}/calmodulin-dependent kinase II (CaMKII α, δ, and γ isoforms), cAMP-dependent protein kinase (PKA; catalytic α subunit), phosphorylase b (γ subunit), Aurora kinase A (AurA), and casein kinase I (CK1 δ, ϵ, and γ-2 subunits; Fig. 8 A).

Having identified candidate kinases, we next tested if their activity is specific to the conserved residues in the HVR by analyzing various mutant ATL1 proteins. Kinase reactions as described above were conducted with the following ATL1 proteins: WT, $S^{10}A$, $S^{22}A/S^{23}A$, $S^{10}A/S^{22}A/S^{23}A$, and ΔHVR. Results are presented as the phosphorylation percentage when compared with WT ATL1. Phosphorylation of S^{10} was specifically catalyzed by p21-activated kinases (PAK7/5, PAK6, and PAK4; Fig. 8 B), Aurora A, and PKA C-α (Fig. 8 C). Phosphorylation of S^{22}/S^{23} was specific to CK2 (both α and α'; Fig. 8 D) and partially to CaMKII (γ, δ, and α; Fig. 8 E). Other kinases appeared less specific, with CK1 δ uniquely phosphorylating the HVR but devoid of apparent residue specificity. CK1 ϵ, CK1 γ-2, and phosphorylase B γ largely

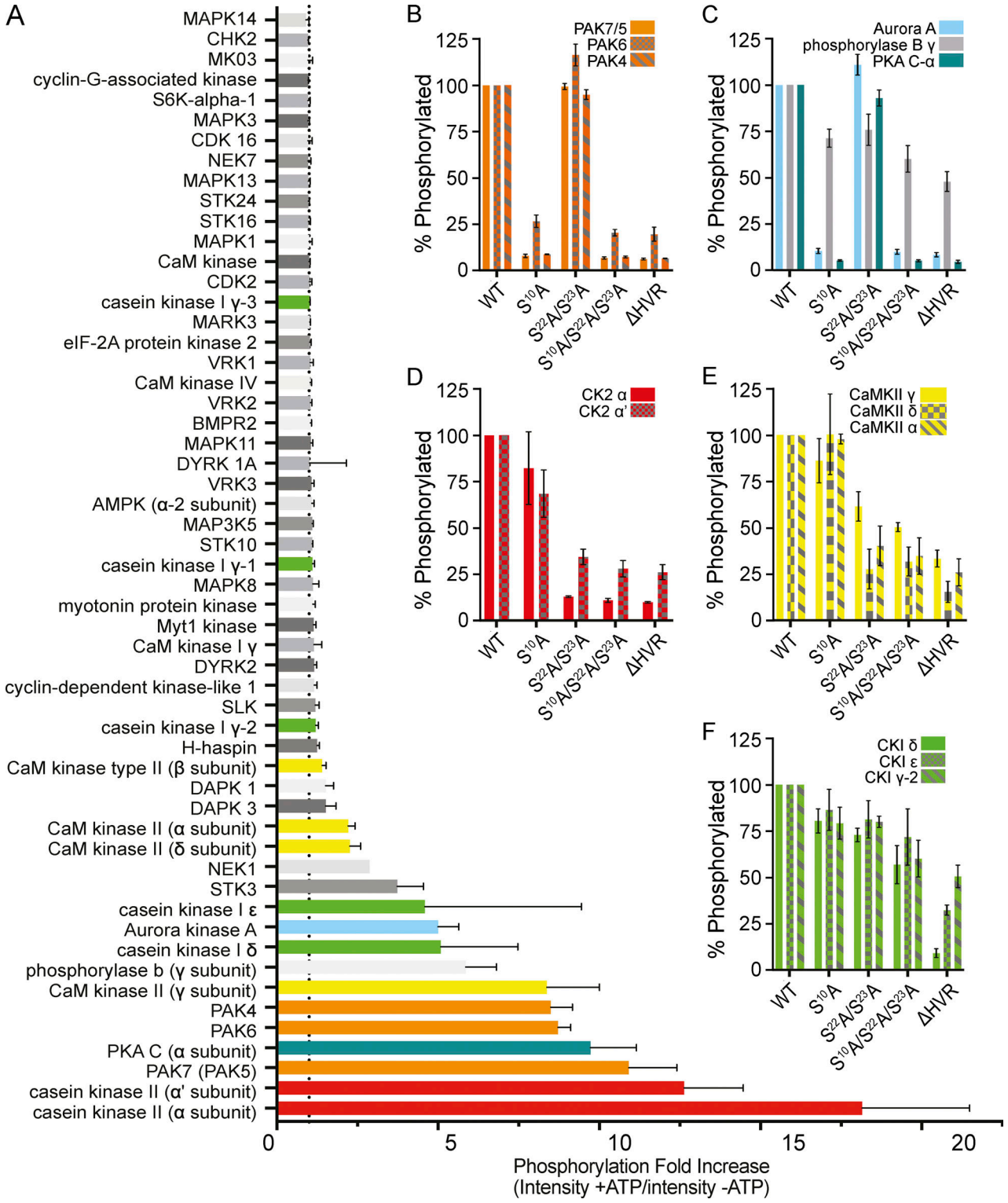

Figure 8. **Kinase screen identifies enzymes that phosphorylate ATL1's HVR site-specifically in vitro. (A)** Kinase reactions were performed using a screen of S/T kinase domains with the ATL1^{6xHIS} catalytic core as the substrate. All reactions were performed in triplicate, run on SDS-PAGE gels, stained with ProQ Diamond phosphoprotein stain, and the band intensity was quantified using ImageJ (Schneider et al., 2012). The phosphorylation fold-increase (plotted on the x axis) was determined by the ratio of band intensity for the +ATP condition over the −ATP condition and plotted as the mean intensity from triplicate conditions (n = 3; error bars show SD). Bars are colored by kinase family where relevant. **(B–F)** In vitro phosphorylation reactions as in A but with mutant ATL1 constructs (biologically relevant S-to-A combinations and ΔHVR) using a subset of kinase candidates identified in A: (B) PAK7/5, PAK6, and PAK4; (C) miscellaneous kinases (AurA, phosphorylase B gamma, and PKA P-α); (D) CK2 α and CK2 α'; (E) CaMKII γ, CaMKII δ, and CaMKII α; and (F) CK1 δ, CK1 ε, and CK1 γ-2. All quantifications are displayed as the average percent of WT ATL1 phosphorylation across triplicate reactions (n = 3; error bars show SD).

phosphorylated regions of the protein within the HVR but also outside of the HVR without any obvious residue specificity (Fig. 8, C and F). Together, these results implicate a subset of kinases capable of phosphorylating ATL1's HVR in a site-specific manner, suggesting biological pathways that involve ATL1 post-translational modifications.

Discussion

Here we provide first structural insights into the short, hypervariable N-terminal region of ATLs, with ATL1's HVR forming a β-hairpin, and ATL3's HVR forming an α-helix (Fig. 1). While short, these motifs are well-conserved across homologues for each ATL isoform but are highly variable across isoforms. The ATL1 HVR could potentially participate in intermolecular protein interfaces, e.g., with a small groove on the side of an adjacent G domain as seen in the crystal lattice. Such packing manifests as long rows of protomers, which, if extrapolated to a set of trans membranes, would support a model in which the HVR works to coordinate aligned ATL1 protomers on the cis membrane in an optimal orientation to dimerize with aligned protomers on the trans membrane. The implications in membrane fusion would be twofold: (1) increased process efficiency through a potential avidity effect, with hydrolysis and subsequent dimerization cycles likely to occur in a primed and/or coordinated manner and interactions potentially spanning longer length scales; and (2) reduction of futile cis hydrolysis cycles, as the orientation of the coordinated polymer would not allow it. The ATL3 HVR structure did not support a similar organization. A HVR-dependent vesicle tethering component observed for ATL1 but not ALT3 supports the hypothesis that ATL1's HVR provides a cooperative benefit when the protein is confined to the two-dimensional space of a membrane, while ATL3's HVR may not function in the same manner.

Based on these isoform effects, we hypothesize that the HVR may have divergent functions in different isoforms. With ATL isoforms retaining such a high overall sequence identity, study of each HVR could shed light on observed discrepancies among the isoforms, including innate kinetic and cellular fusion efficiencies (Hu et al., 2015; O'Donnell et al., 2017) as well as roles in other cellular pathways such as ER-phagy (Liang et al., 2018; Chen et al., 2019), lipid droplet formation (Klemm et al., 2013; Falk et al., 2014), and viral and bacterial proliferation (Shen et al., 2017; Steiner et al., 2017; Monel et al., 2019; Neufeldt et al., 2019). Future studies may also look at whether the HVR functions in isoform segregation, as most cell types express multiple ATL isoforms (Rismanchi et al., 2008), and it is not known whether mixed-isoform dimers or oligomers are functional. A recent study demonstrated isoform-specific roles of ATLs in supporting replication of dengue and Zika virus in infected cells, implicating the HVR in this process (Neufeldt et al., 2019). In this context, it also was posited that the HVR may confer isoform specificity in regard to functional homodimerization in the cell, a model our present study may support.

Regulation for dynamin-catalyzed membrane fission involves recruitment to growing helical dynamin polymers at stalks of budding vesicles (Antonny et al., 2016; Jimah and Hinshaw, 2019) and stimulation of GTP hydrolysis rates upon polymerization (Tuma and Collins, 1994; Warnock et al., 1996; Chappie et al., 2010; Kong et al., 2018; Chappie et al., 2009; Ford and Chappie, 2019), mechanisms that are not directly evident in ATL-catalyzed membrane fusion. One may expect oligomerization patterns to deviate between fission and fusion events, especially considering that homotypic fusion inherently necessitates interactions of two protein populations: those on cis versus trans membranes. While a majority of the research on ATL's catalytic mechanism has focused on how trans interactions contribute to membrane fusion, much remains unknown regarding cis interactions (Liu et al., 2015). Accumulating evidence supports the crucial role such interactions play in dynamin-related fusion proteins. Mitofusins (Mfns), which are responsible for homotypic fusion of outer mitochondrial membranes, undergo cis oligomerization in a redox- and GTP-dependent manner, which increases mitochondrial fusion efficiency (Shutt et al., 2012; Mattie et al., 2018). More strikingly, cryo-electron tomography experiments have shown that Mfns form a more clustered array at the docking site of opposing membranes, which, with multiple rounds of GTP hydrolysis, is proceeded by formation of fusion pores (Brandt et al., 2016). Visualization of ATL-containing, docked proteoliposomes by electron microscopy has revealed that an ATL tether-trapping (nonfusogenic) mutation exhibited a zipper-like ultra-structure at the vesicle interface (Saini et al., 2014), strongly suggesting prefusion coordination of ATLs. The HVR-dependent cis/trans oligomer model proposed here for human ATL1 suggests one structural solution, by which formation of ATL oligomeric arrays could provide cooperative improvements to membrane fusion efficiency.

Post-translational modifications of dynamin provide an additional level of control of membrane fusion events (Smillie and Cousin, 2005; Kar et al., 2017; Srinivasan et al., 2018; Ahn et al., 2002; Cao et al., 2010). ATL1 phosphorylation occurs in mammalian cells on residues S^{10}, S^{22}, and S^{23}, with S^{10} being modified in 100% of identified peptides, and $S^{22/23}$-containing peptides existing either doubly phosphorylated or doubly unphosphorylated (Fig. 4, C and D). Mass spectroscopy experiments performed on ATL1 serine-to-alanine mutant proteins established that while S^{10} remains completely phosphorylated in the absence of S^{22}/S^{23} phosphorylation, S^{22}- and S^{23}-containing peptides are variably phosphorylated within a $S^{10}A$ mutant protein (Fig. 7). This could result from alteration of kinase binding or recognition site(s) or downstream signaling events due to the absence of S^{10} phosphorylation. Similar to the HVR deletion, $S^{10}E$ mutation mimicking HVR phosphorylation at this site resulted in a significant decrease in tethering rates (Fig. 5, B and C), with the effect being specific to the phosphomimetic mutation, as the corresponding serine-to-alanine mutant proteins were unaffected (Fig. S3). Although our mass spectroscopy results indicated that S^{10} was completely phosphorylated in mammalian cell–derived samples, immunofluorescence experiments revealed that expression of either the ATL1 phosphomimetic $S^{10}E$ or the $S^{10}A$ control mutant resulted in redistribution from ER tubules to puncta (Fig. 6, B and E). This is suggestive of a crucial turnover of this modification, even if transient or within small subpopulations of the protein. Together with the delayed tethering kinetics, one functional mode for the

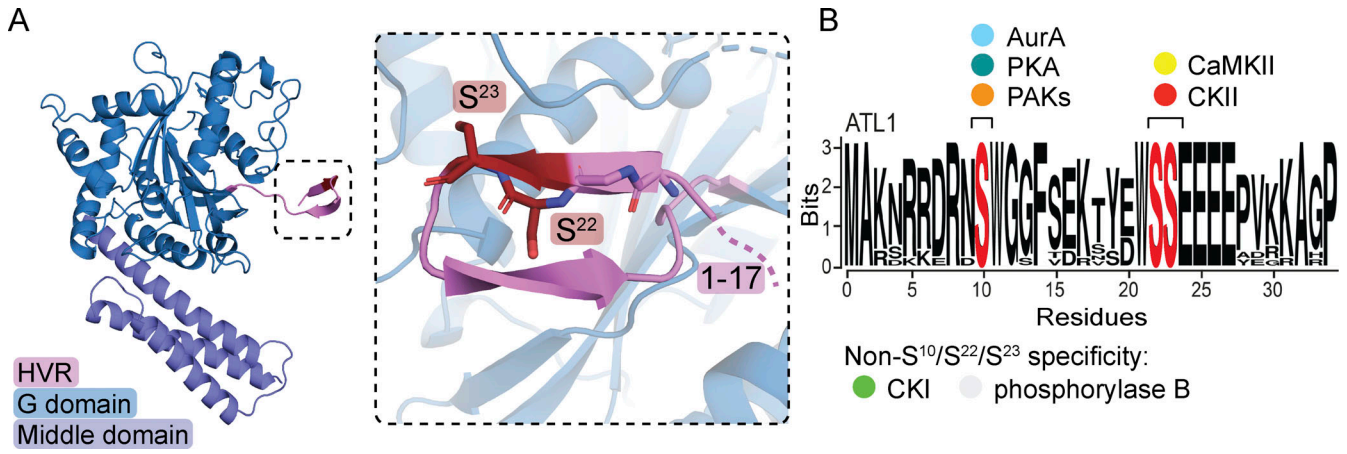

Figure 9. **Phosphorylation of conserved serine residues in the ATL1 HVR. (A)** Cartoon representation of the ATL1 catalytic core structure presented in Fig. 1 (G domain, blue; middle domain, purple; structured portion of the HVR spanning residues 18–31, pink; S^{22} and S^{23}, red; residues 1–17, disordered). The inset shows a close-up view of the HVR with S^{22} and S^{23} side chains and main chain represented as sticks and colored in red and according to atom type. **(B)** WebLogo of the ATL1 HVR with the conserved serine residues found to be phosphorylated shown in red. Above the phosphorylated residues are listed their cognate kinase candidates. Less specific kinase candidates are listed below.

phosphorylation could be in regulating turnover of ATLs by priming for subsequent hydrolysis through regulation of HVR structure and/or interactions. A similar mechanism was identified for the regulation of mitochondrial fusion by ubiquitination of Mfns, found to alter its oligomerization state (Anton et al., 2013). However, as our ATL1 HVR structure begins at residue 18, any model remains speculative at this point.

Unlike with the ATL1 S^{10} mutants, expression of ATL1 $S^{22}E/S^{23}E$ and $S^{22}A/S^{23}A$ mutant proteins in mammalian cells yielded different phenotypes, with expression of the $S^{22}E/S^{23}E$ mutant causing a decrease in the percentage of cells with discernible ATL1-positive tubules and an increase of cells lacking distinct boundaries of ATL1 signal localization ("fuzzy" signal), while expression of the $S^{22}A/S^{23}A$ mutant protein presented as ATL1 WT (Fig. 6, C, E, and F). As the effects were specific to the mimicked phosphorylation state, modification of S^{22} and/or S^{23} appears to result in a more binary regulatory mode, with little impact on tethering kinetics (Fig. 5). As S^{22} and S^{23} are located within the first β-sheet of the HVR and near the turn of the hairpin, phosphorylation of these residues may influence its secondary structure and/or electrostatic potential (Fig. 9 A). While the mechanism of how this translates to cellular activity and ER sub-localization is not yet clear, the regulatory mode appears to deviate from that of S^{10} phosphorylation. When the ATL1 triple phosphomimetic mutant and corresponding alanine control ($S^{10}E/S^{22}E/S^{23}E$ or $S^{10}A/S^{22}A/S^{23}A$) were expressed in cells, phenotypes appeared to more strongly match those seen with S^{10} mutants (Fig. 6, D–F). Along with our mass spectroscopy and kinetic data, this indicates that S^{10} phosphorylation retains a dominant effect over S^{22} and/or S^{23} modification. The identification of kinases (and phosphatases) carrying out these modifications may help uncover the biological implications of ATL1 regulation through phosphorylation. Our studies revealed several candidate families that showed site-specific effects and share localization and/or common processes with ATLs (Fig. 9 B).

CK2 α and α' catalytic subunits were the two top hits, modifying ATL1 primarily on residues S^{22} and/or S^{23} (Fig. 8 D). CK2 is implicated in cell survival and progression, linked to ER stress levels (Venerando et al., 2014) and neuronal development (Blanquet, 2000). Both ATL1 and CK2 are primarily expressed in the brain (Blanquet, 2000), and α, α', and β subunits localize to the smooth ER (Faust et al., 2001).

S^{10}-specific kinases include the group II p21-activited kinases (PAK7/5, PAK6, and PAK4), AurA, and PKA. Group II PAKs regulate cytoskeletal dynamics, cell survival, proliferation, and neuronal development with mutations leading to neurodegenerative disease (Kumar et al., 2017; Eswaran et al., 2008). AurA is a particularly strong candidate for phosphorylation of S^{10} as it was the subject of one of the large, unbiased screens initially reporting phosphorylation on this ATL1 residue (Kettenbach et al., 2011). AurA plays a critical role in mitotic progression through centrosome maturation, formation of bipolar spindles, and coordination of cytokinesis (Nikonova et al., 2013). It is well established that the distribution of the ER throughout the cell periphery is closely linked to microtubule cytoskeletal dynamics (Terasaki et al., 1986; Park et al., 2010) and that during mitosis, the ER undergoes drastic morphological changes (Puhka et al., 2007; Wang et al., 2013; McCullough and Lucocq, 2005), which ATL helps regulate (Wang et al., 2013). Phosphorylation of ATL1 by AurA would be a novel mechanism through which ER morphology is controlled through the cell cycle. This could mirror conceptually a mechanism identified for controlling mitochondrial dynamics during the G2/M phase via the phosphorylation of the dynamin-related Drp1 homologue, important for fission, through an AurA homologue (Kato et al., 2019).

The catalytic subunit of PKA also modifies ATL1 on S^{10} in vitro. This kinase is activated upon increases in cellular concentration of cAMP in response to diverse signaling events, including activation of G protein coupled receptors (Turnham and Scott, 2016). Several studies have reported regulation of mitochondrial dynamics by PKA by phosphorylation of Drp1

(Chang and Blackstone, 2007; Cribbs and Strack, 2007) and Mfn2 (Zhou et al., 2010), suggesting a common theme in regulating organelle dynamics. Several CaMKII isoforms (γ, δ, and α) phosphorylate ATL1, primarily on S^{22} and/or S^{23}, although there is also apparent modification outside of the HVR. CaMKII plays a crucial role in learning and memory formation putatively by promoting long-term potentiation in dendritic spines (Lisman et al., 2002). A number of reports have identified functional phosphorylation of Drp1 by CaMKII, resulting in altered mitochondrial morphology (Xu et al., 2016; Hu et al., 2019; Bo et al., 2018; Jiang et al., 2015). A recent study presented a direct connection between CaMKII and somatosensory-activated disruption of ER structure in murine neurons, implicating a dynamin-related protein in restoring a continuous ER (Kucharz and Lauritzen, 2018). Although speculation at this point, ER collapse and recovery through a reversible, CaMKII-mediated phosphorylation of ATL1 could provide a plausible model for this observation.

While ATL1 regulation by phosphorylation has not yet been reported in humans, it has been described for its *Arabidopsis thaliana* homologue root hair defective 3 (RHD3), in which C-terminal phosphorylation events increased membrane fusion activity by promoting oligomerization (Ueda et al., 2016). Additionally, both RHD3 and human ATL1 are regulated by ubiquitylation modifications altering protein levels through targeted protein degradation (Sun et al., 2020) or decreased GTPase activity (Zhao et al., 2020), respectively.

Based on evidence we have shown here, it appears that ATL1's HVR encodes innate aspects of the enzyme's tethering efficiency and potentially membrane fusion. We have laid the groundwork for better understanding of how this ill-defined motif contributes to regulation of ATL1 intrinsically through putative inter-molecular interactions and extrinsically through phosphorylation of conserved serine residues by candidate kinases identified here. Future work may expand upon these models and continue to define how ATL function is regulated, especially in the context of the majority of cells that express more than one isoform with distinct HVRs, allowing for distinct control. It will also be interesting to explore how the features described here may play into the dynamic remodeling of the ER during cell division and in other pathways in which ATLs have been implicated.

Materials and methods

Primers

The following DNA oligos, synthesized by Thermo Fisher Scientific, were used in the studies (for site-directed mutagenesis, only sense primers are listed; corresponding reverse-complement primers were used in the mutagenesis PCR): ATL1_pET21_1_s, 5′-GATATCGCTAGCATGGCCAAGAACCGCAGGGAC-3′; ATL1_pET21_33_s, 5′-GATATCGCTAGCATGGGTCCGGTTCAGGTTCTGATTGTG-3′; ATL1_pET21_439_as, 5′-GATATCGCGGCCGCTTTGCTATCATTGTGCTTGAT-3′; ATL1_pET21_449_as, 5′-CTCGAGGCGGCCGCTTACATTTTTTTTTTTCTCGCTCTGTTCG-3′; ATL3_pET21_1_s, 5′-GATATCGCTAGCATGTTGTCCCCTCAGCGAGTGG-3′; ATL3_pET21_25_s, 5′-GATATCGCTAGCATGGGTCCAGTGCAGGTTGTTTTGGTTC-3′; ATL3_pET21_334_as, 5′-GATATCGCGGCCGCCCTTGATAAATTTTAATATATG-3′; ATL3_pET21_445_as, 5′-CTCGAGGCGGCCGCCTATTGAGCTTTTTTATCCATGGATGG-3′; ATL1_pcDNA_1_s, 5′-GATATCGGATCCATGGCCAAGAACCGCAGGGAC-3′; ATL1_pcDNA_33_s, 5′-GATATCGGATCCATGGGACCAGTCCAAGTCCTCATTG-3′; ATL1_pcDNA_558_as, 5′-GATATCGCGGCCGCCATTTTTTTCTTTTCTGATTG-3′; ATL1S10A_s, 5′-CAAGAACCGCAGGGACAGAAACGCTTGGGGTGGATTTTCGGAAAAG-3′; ATL1S^{22}A_s, 5′-GGAAAAGACATATGAATGGGCCTCAGAAGAGGAGGAGCCAGTG-3′; ATL1S^{23}A_s, 5′-GGAAAAGACATATGAATGGAGCGCAGAAGAGGAGGAGCCAGTG-3′; ATL1$S^{22/23}$A_s, 5′-GGAAAAGACATATGAATGGGCCGCAGAAGAGGAGGAGCCAGTG-3′; ATL1S^{10}E_s, 5′-CAAGAACCGCAGGGACAGAAACGAATGGGGTGGATTTTCGGAAAAG-3′; ATL1S^{22}E_s, 5′-GGAAAAGACATATGAATGGGAGTCAGAAGAGGAGGAGCCAGTG-3′; ATL1S^{23}E_s, 5′-GGAAAAGACATATGAATGGAGCGAGGAAGAGGAGGAGCCAGTG-3′; and ATL1$S^{22/23}$E_s, 5′-GGAAAAGACATATGAATGGGAGGAAGAAGAGGAGGAGCCAGTG-3′.

Protein expression and purification

The catalytic core with or without the N-terminal hypervariable motif of human ATL1 (1–449 and 33–449) and ATL3 (1–445 and 25–445) was cloned into a pET21 vector with a C-terminal decahistidine tag using standard molecular cloning methods. The catalytic core of ATL1 (residues 1–439) and the G domain of ATL3 (residues 1–334) with a C-terminal hexahistidine tag were expressed from a pET21 vector. Overexpression of each construct was performed using *Escherichia coli* BL21(DE3) upon induction with 0.5 mM IPTG at 18°C for 16 h. Cells were harvested by centrifugation at 4,500 ×*g* and resuspended in Ni^{2+}- nitrilotriacetic acid (NTA) Buffer A (25 mM Tris-Cl, pH 8.5, 500 mM NaCl, and 20 mM imidazole), snap-frozen in liquid nitrogen, and stored at −80°C. To purify, cells were thawed at room temperature, sonicated, and spun at 39,000 ×*g* to remove membrane aggregates. Supernatant was loaded onto Ni^{2+}-NTA Superflow resin (Qiagen) at 1 ml resin per 1 liter culture. Flow-through was discarded, and resin was washed with 15 column volumes (CV) buffer A followed by elution with Ni^{2+}-NTA buffer B (25 mM Tris-Cl, pH 7.5, 500 mM NaCl, and 500 mM imidazole) in 3 CV. Protein was desalted using a HiPrep 26/10 Desalting column (GE Life Sciences) into buffer containing 25 mM Tris-Cl, pH 7.5, 400 mM NaCl, and 5 mM EDTA. Desalted protein was concentrated with a 30,000 MWCO filter protein concentrator (Millipore) and gel-filtered on a GE S200 16/60 column equilibrated in 25 mM Tris-Cl, pH 7.5, and 100 mM NaCl. Peak fractions were concentrated and snap-frozen in liquid nitrogen and stored at −80°C.

Crystallization of ATLs

All ATL crystals were attained by initial sitting drop vapor diffusion screening and optimized via hanging drop vapor diffusion by mixing 1 µl of protein and 1 µl of reservoir solution followed by incubation at 20°C. For ATL1 residues 1–439, crystals grown from either native or selenomethionine-derivatized protein were attained from a 30 mg/ml protein solution containing 2 mM guanosine-5′-[(β,γ)-methyleno]triphosphate (Jena Biosciences) and 4 mM $MgCl_2$, and a reservoir solution containing 3.5 M sodium formate, pH 7. For ATL3 residues 1–334, crystals

were attained from a 20 mg/ml protein solution containing 2 mM guanosine 5′-diphosphate (Sigma-Aldrich) and 4 mM $MgCl_2$, and a reservoir solution containing 187.5 mM ammonium acetate, 21.5% PEG3350, and 100 mM Bis-Tris, pH 6.5. Crystals were transferred to reservoir solution supplemented with 25% glycerol for cryoprotection and flash-frozen in liquid nitrogen.

Crystallographic data collection and analysis

Data were collected on ATL1 and ATL3 crystals using Cornell High Energy Synchrotron Source (CHESS) beamlines A1 and F1, respectively. For ATL1, single anomalous diffraction experiments were conducted on selenomethionine-containing proteins for experimental phasing. ATL1 datasets were collected at lambda = 0.9767 Å with 1° oscillations on an ADSC Q210 CCD area detector. For ATL3, data were collected at lambda = 0.9770 Å with 1° oscillations on a Pilatus 6M detector. Images were integrated and scaled using XDS and XSCALE for all datasets (Kabsch, 2010). The ATL1 selenomethionine data were truncated at 3.5 Å where the anomalous correlation was calculated to be 18% in the high-resolution bin. Substructure and phases were attained through Autosol (Terwilliger et al., 2009) using the selenomethionine data for phase information and native data for high resolution reflections. Phases for ATL3 were attained through molecular replacement methods using PHENIX (Liebschner et al., 2019) and the coordinates of ATL3 (PDB accession no. 5VGR) as the search model. All structures were subsequently built and refined against the native datasets using PHENIX (Liebschner et al., 2019) and Coot (Emsley et al., 2010). The aforementioned software packages were accessed through SBGrid (http://www.sbgrid.org; Morin et al., 2013).

Phosphate release kinetics

GTP hydrolysis activity for all ATL catalytic core constructs was determined using the Enzchek phosphate assay kit from Thermo Fisher Scientific. Reactions were scaled to a final volume of 200 µl with a total concentration of 0.5 mM GTP (Thermo Fisher Scientific). Reactions contained a range of ATL concentrations, from 0 µM to 2 µM, run in the presence of reaction buffer (25 mM Tris-Cl, pH 7.5, 100 mM NaCl, and 2 mM $MgCl_2$). Starting at the time of GTP addition, release of P_i was measured as a spectrophotometric shift from 330 to 360 nm with the conversion of 2-amino-6-mercapto-7-methylpurine riboside to ribose 1-phosphate and 2-amino-6-mercapto-7-methylpurine by purine nucleoside phosphorylase. k_{cat} values were calculated using three technical replicates and two biological replicates for each protein construct.

SEC-MALS

The catalytic core constructs of ATL1 and ATL3 with and without their HVR used for kinetic experiments were loaded onto a Superdex Increase 200 10/300 GL column (GE) at 50 µM after column equilibration with MALS buffer (25 mM Tris-Cl, pH 7.5, 100 mM NaCl, 2 mM EGTA, and 4 mM $MgCl_2$), run at 0.7 ml/min. ATL WT and mutant protein constructs were first incubated with indicated nucleotides (2 mM GDP, 2 mM guanosine 5'-[β,γ-imido]triphosphate (GppNHp), 2 mM GDP in the presence of 2 mM $AlCl_2$, 20 mM NaF, and 4 mM EGTA, or without nucleotide). After column separation, protein was run through a static 18-angle light scattering detection unit (DAWN HELEOS-II) and a refractive index detector (Optilab T-rEX). Determination of molecular mass was calculated using Wyatt's Astra VI software. Monomeric BSA (Sigma-Aldrich) was used to normalize signal intensity across light-scattering detectors.

SEC-SAXS

Experimental set-up was exactly as described in SEC-MALS section. Data were collected at CHESS at the BioSAXS beamline (Beamline ID7A1). Background signal was established as baselined scattering signal at the beginning of each SEC run, within the void volume of the column (after buffer equilibration). All data were processed using the ATSAS suite (Manalastas-Cantos et al., 2021) and BioXTAS RAW (Hopkins et al., 2017). Frames from monodisperse peak maxima (determined by x-ray scattering intensity and absorbance intensity at 280 nm) were averaged for analysis. Guinier analysis was performed to assess quality of the experimental data, with a maximum $qR_g < 1.3$ (q, scattering angle; R_g, radius of gyration). Indirect Fourier transform of experimental data yielded the distance distribution plot, or P(r). Kratky plots were derived from P(r) functions and report protein foldedness.

Liposome preparation

Lipids were purchased from Avanti Polar Lipids either reconstituted in chloroform or as desiccate and subsequently reconstituted after purchase. For liposome tethering and flotation assays, lipids were prepared at 10 mM at a molar ratio of 1% 18:1 DGS-NTA(Ni) (1,2-dioleoyl-*sn*-glycero-3-[(N-(5-amino-1-carboxypentyl)iminodiacetic acid)succinyl]) to 99% 18:1 (Δ9-cis) PC (1,2-dioleoyl-*sn*-glycero-3-phosphocholine) by transferring indicated molar amounts of each lipid to glass vials and evaporating chloroform under an N_2 air stream for 15–20 min, then desiccating for 1.5 h. Multilamellar vesicles were produced by reconstituting lipids in reaction buffer (25 mM Tris-Cl, pH 7.5, and 100 mM NaCl) with intermittent vortexing for 30 min. Multilamellar vesicles were subjected to 10 freeze-thaw cycles between liquid N_2 and a 25°C water bath to reduce multilamellar structures in favor of unilamellar vesicles. Liposomes were stored at −80°C until needed. Liposomes were thawed at room temperature, then extruded to establish a homogenous population size of unilamellar vesicles by extruding samples through a 100-nm filter 21 times and used immediately.

Liposome tethering assay

Catalytic core ATL protein was loaded onto extruded vesicles as a 2X reaction stock with 2 mM lipids (1 mM final) and 2–5 µM protein (1–2.5 µM final) by incubating at room temperature for 30 min. Reactions were initiated by dilution of 2X reaction stock with reaction buffer (25 mM Tris-Cl, pH 7.5, 100 mM NaCl, and 4 mM $MgCl_2$) either in the presence or absence of 500 µM GTP. Reactions were measured spectrophotometrically at OD_{360} for 45 min and were imaged at t = 45 min using a BioRad Chemidoc system. Each reaction condition was performed in triplicate with two biological replicates, and all data analysis was done in GraphPad Prism. For each triplicate condition, the signal from

the reactions lacking GTP was averaged and subtracted from the reactions containing GTP. For calculating apparent tethering rates, data were truncated after the signal plateaued at the maximum and before the signal dropped off (only in conditions where a drop-off in signal was observed). A single-phase association rate was fitted to each replicate, then averaged and plotted against protein concentration. The rate constant for each protein construct was determined by calculating the linear regression of rates versus protein concentration. An unpaired *t* test was performed to determine statistical significance.

Statistical analysis

Unless otherwise indicated, all kinetic reactions were performed in triplicate with two biological replicates (n = 6). Biological replicates used recombinant protein expressed and purified separately. Statistical significance was calculated to compare ATL1 WT with mutant proteins in GTPase and vesicle tethering assays using unpaired, two-tailed *t* tests with significance indicated by a P value <0.05. For cell imaging experiments, experiments were performed in triplicate. Percentages of imaged cells with a given phenotype were calculated for each experimental condition. Statistical significance of phenotype changes compared with ATL1 WT and cognate mutant pairs (e.g., ATL1 $S^{10}E$ and ATL1 $S^{10}A$) was determined using one-way ANOVA analysis. Normal distribution of data was assumed but not formally tested.

Liposome flotation assay

Flotation assays were conducted using a Nycodenz concentration gradient as described by Liu et al. (2015). Nycodenz stock solutions were prepared at 25% and 70% in tethering reaction buffer. 2X liposomes stocks were prepared and loaded with ATL as described above at 2 µM protein and 2 mM lipids. The 2X loaded vesicle stock was combined at a 1:1 ratio with the 70% Nycodenz solution, for a final mixture composed of 35% Nycodenz, 1 µM protein, and 1 mM lipids. This solution comprised the bottom 20% of the total volume of concentration gradient. The middle 70% of the gradient consisted of the 25% Nycodenz solution, and the top 10% of the volume was composed of vesicle tethering reaction buffer. The gradients were spun for 2 h at 200,310 ×*g* at 4°C. Fractions were taken from the top, middle, and bottom for analysis on SDS-PAGE by SYPRO Ruby staining (Thermo Fisher Scientific).

Cell lines and antibodies

The following cells were used in experiments as indicated: U2OS (American Type Culture Collection ID HTB-96); NIH-3T3 (American Type Culture Collection ID CRL-1658) were received from Dr. Craig Blackstone's laboratory (National Institute of Neurological Disorders and Stroke, Bethesda, MD); NIH-3T3 ATL1/2/3 TKO cells (E21 cell line) were engineered by the Blackstone laboratory using CRISPR editing, resulting in each *atl* allele having small insertion or deletion mutations (1–7 nt) in exon regions (described in Zhao et al., 2016). The following antibodies were used as indicated in subsequent sections: anti-c-Myc monoclonal antibody (mouse) 9E10 (Thermo Fisher Scientific; cat #MA1-980); anti-calnexin polyclonal (rabbit; Abcam; cat #ab22595); EZview Red anti-c-Myc (rabbit) affinity gel (Sigma-Aldrich; cat #E6654); Goat anti-mouse IgG cross-adsorbed secondary antibody, Alexa Fluor 488 (Thermo Fisher Scientific; cat #A-11017); goat anti-mouse IgG (heavy and light chains) HRP-conjugated secondary antibody (Thermo Fisher Scientific; cat #62-6520); and goat anti-rabbit IgG (heavy and light chains) HRP-conjugated secondary antibody (Thermo Fisher Scientific; cat #65-6120).

Mass spectroscopy

ATL1 (1–558) WT, $S^{10}A$, $S^{22}A/S^{23}A$, and $S^{10}A/S^{22}A/S^{23}A$ were cloned into a pcDNA4 mammalian expression vector containing a C-terminal c-myc tag using standard molecular cloning techniques. U2OS cells were transiently transfected using polyethylenimine and harvested after 24 h by washing three times in cold PBS. Cells were lysed in 25 mM Tris-Cl, pH 7.5, 100 mM NaCl, and 1% Triton X-100. Cleared lysates were loaded onto EZview Red α-c-myc affinity resin preequilibrated in wash buffer (same as lysis buffer but with 0.1% Triton X-100) and incubated, rotating at 4°C for 2 h. The supernatant was removed, and the resin was washed three times with wash buffer for 15 min each. Protein was eluted in 0.1 M glycine, pH 2.5, by incubating for 10 min, followed by pH adjustment to pH 7.5 with Tris-HCl. All buffers used in sample processing contained Halt protease and phosphatase inhibitor cocktail (Thermo Fisher Scientific), except for the last resin wash step and elution buffer. Samples were cleaved with trypsin following elution, then applied to LC-MS/MS for analysis.

Western blot analysis

As described above, all mammalian expression vectors contained a C-terminal c-myc tag. Transfections in U2OS cells were performed with polyethylenimine, and transfections in NIH-3T3 ATL1/2/3 TKO cells were performed using Avalanche-Omni (EZ Biosystems) according to the manufacturer's instructions. Cells were washed three times in cold PBS, then harvested by scraping and lysed in cold lysis buffer containing either Halt protease and phosphatase inhibitors or cOmplete protease inhibitors (Millipore Sigma), depending on the experiment. After clearing aggregates by centrifugation, total lysate protein concentration was determined by Bradford reagent (Bio-Rad), and samples were normalized before loading on either SDS-PAGE or Phos-tag gels (FujiFilm WAKO) and run according to the manufacturer's instructions, followed by transfer to polyvinylidene difluoride membranes. Before transfer, Phos-tag gels were washed in transfer buffer containing 10 mM EDTA a total of three times for more efficient protein transfer. Polyvinylidene difluoride blots were blocked either overnight at 4°C or at room temperature for 2 h using SuperBlock T20 (TBS) Blocking Buffer (Thermo Fisher Scientific). Blots were incubated either with 1:1,000 mouse α-c-myc monoclonal 9E10 antibody (Thermo Fisher Scientific) or 1:60,000 rabbit α-calnexin (Abcam) in TBS with 0.1% Tween-20 for 1 h at room temperature, followed by a 30-min incubation period with either 1:5,000 goat α-mouse-HRP polyclonal antibody or 1:5,000 goat α-rabbit-HRP polyclonal antibody (Thermo Fisher Scientific) diluted in TBS with 0.1% Tween-20. Blots were washed three times with PBS between

antibody incubation steps. Blots were developed with enhanced chemiluminescent HRP substrate (Thermo Fisher Scientific) and imaged with a ChemiDoc XRS+ System (BioRad).

Mammalian cell immunofluorescence and imaging

NIH-3T3 ATL1/2/3 TKO and U2OS cells were seeded in Nunc Lab-Tek chamber slides, transfected as described above, and processed 24 h after transfection. Cells were washed three times with cold PBS, then fixed with 4% formaldehyde for 20 min followed by permeabilization with 0.1% Triton X-100 in PBS for 10 min, then blocked in 10% BSA in PBS for 2 h. Cells were incubated with primary antibody for 1.5 h in a 5% BSA PBS solution containing 1:400 mouse α-c-myc monoclonal antibody, then washed and incubated with a 1:400 dilution of secondary antibody of α-mouse Alexa Fluor 488 (Invitrogen) for an hour. Cells were washed a final set of times and treated with ProLong Gold Antifade mountant (Thermo Fisher Scientific), then sealed with a coverslip. Imaging was performed at 25°C on a Perkin-Elmer UltraView spinning disc confocal microscope with a Nikon Plan Apo 60×A/1.4 oil objective using a 1394 ORCA-ER camera (Hamamatsu Photonics) and Ultraview software (Perkin-Elmer).

Image brightness and contrast were adjusted using ImageJ (Schneider et al., 2012). Each image was scored on the presence or absence of apparent tubule and/or puncta localization of ATL as well as whether the ATL signal was diffuse ("fuzzy") throughout the cell. These phenotypes were not mutually exclusive. For each condition, a minimum of 70 cells was imaged across three experiments and categorized (with the exception of ATL1 WT with 44 cells). Statistical comparisons were determined using one-way ANOVA, with significance defined as $P < 0.05$.

Kinase screen expression and purification

Kinase screen (Addgene kit #1000000094) was received as bacterial glycerol stocks. Expression and purification protocols were adapted from the published protocol in Albanese et al. (2018). Plasmids containing all the Ser/Thr kinases were isolated by miniprep of overnight cultures inoculated from glycerol stocks. Plasmids containing kinases conferred carbenicillin resistance and were cotransformed into Rosetta2 DE3 cells (Novagen) with a lambda phosphatase-encoding plasmid conferring resistance for spectinomycin (provided in the Addgene kit). 60 ml cultures containing MagicMedia (Invitrogen), 100 µg/ml carbenicillin, and 100 µg/ml spectinomycin were inoculated with Rosetta2 DE3 cotransformations and grown at 37°C for 4 h, then at 16°C for 40 h. Cells were harvested by centrifugation at 3,000 ×*g*, resuspended in buffer A, and frozen in liquid N_2. Frozen cell pellets were thawed to room temperature followed by sonication on ice until lysates were homogenous. Lysates were cleared by centrifugation at 3,000 ×*g* at 4°C, then loaded onto 100 µl Ni^{2+}-NTA resin (Qiagen) preequilibrated with buffer A. Resin was washed with 100 CV buffer A, then eluted into 250 µl buffer B. Protein concentration was measured by Bradford reagent (BioRad), then aliquoted and frozen in liquid N_2 and stored at −80°C until needed.

In vitro phosphorylation experiments

All kinase reactions were performed in triplicate with a final concentration of 0.5 µM kinase, 20 µM catalytic core ATL substrate, 5 µM ATP, and 1X Halt protease and phosphatase inhibitor (Thermo Fisher Scientific) in a volume of 50 µl in kinase reaction buffer (30 mM Tris-Cl, pH 7.5, 100 mM NaCl, 20 mM $MgCl_2$, and 1 mg/ml BSA). Control reactions were run in the absence of either ATP or ATL substrate. Reactions were run for 1.5 h at room temperature. 10% total reaction volume was analyzed by separation by SDS-PAGE followed by staining with ProQ Diamond phosphoprotein stain (Thermo Fisher Scientific) and imaging with a ChemiDoc XRS+ System (BioRad). Quantification of phosphorylation levels was determined by band intensity quantification in ImageJ (Schneider et al., 2012). In Fig. 8 A, the ratio of ATL1 band intensity in the presence and absence of ATP was reported as an average across triplicate experiments. In Fig. 8 B, phosphorylation levels of ATL1 mutant proteins were reported as a percentage of the ATL1 WT band intensity in the presence of ATP. Values here were also reported as an average across three replicates.

Online supplemental material

Fig. S1 depicts crystal packing, HVR interfaces, and electron density of ligands for both ATL1 and ATL3. Fig. S2 provides vesicle tethering controls, which include ATL3 ± HVR, density gradient centrifugation, and assays supplemented or devoid of EDTA, imidazole, GDP, and $MgCl_2$. Fig. S3 is a mutational analysis of ATL1 serine residues found to be phosphorylated; phosphate release and tethering are assayed. Fig. S4 includes microscopy of mutated HVR phosphorylation sites and the corresponding ER localization. Fig. S5 shows auto-phosphorylation controls and example ProQ Diamond phosphoprotein–stained SDS-PAGE analysis.

Acknowledgments

Mass spectrometry experiments were carried out at the Cornell Biotechnology Resource Center Proteomics and Metabolomics Facility under the guidance of Dr. Sheng Zhang. The plasmid containing Sec61β was received from Dr. Gia Voeltz at University of Colorado, Boulder (Boulder, CO). NIH-3T3 ATL1/2/3 TKO cells were a kind contribution from Dr. Craig Blackstone at the National Institute of Neurological Disorders and Stroke (Bethesda, MD).

This work is based upon research conducted at the CHESS, which is supported by the National Science Foundation and the National Institutes of Health/National Institute of General Medical Sciences under National Science Foundation award DMR-1829070, using the Macromolecular Diffraction at CHESS facility, which is supported by the National Institutes of Health, through its National Institute of General Medical Sciences (award GM-124166). We are grateful for support through a grant (to H. Sondermann) from the Spastic Paraplegia Foundation.

The authors declare no competing financial interests.

Author contributions: C.M. Kelly, H. Sondermann, and J.P. O'Donnell conceptualized the research, analyzed the data, and wrote the manuscript, which was reviewed and edited by all authors. C.M. Kelly, L.J. Byrnes, N. Neela, and J.P. O'Donnell conducted the experiments and prepared the figures.

Submitted: 27 April 2021
Revised: 3 August 2021
Accepted: 2 September 2021

References

Ahn, S., J. Kim, C.L. Lucaveche, M.C. Reedy, L.M. Luttrell, R.J. Lefkowitz, and Y. Daaka. 2002. Src-dependent tyrosine phosphorylation regulates dynamin self-assembly and ligand-induced endocytosis of the epidermal growth factor receptor. *J. Biol. Chem.* 277:26642–26651. https://doi.org/10.1074/jbc.M201499200

Albanese, S.K., D.L. Parton, M. Işık, L. Rodríguez-Laureano, S.M. Hanson, J.M. Behr, S. Gradia, C. Jeans, N.M. Levinson, M.A. Seeliger, and J.D. Chodera. 2018. An open library of human kinase domain constructs for automated bacterial expression. *Biochemistry.* 57:4675–4689. https://doi.org/10.1021/acs.biochem.7b01081

Anton, F., G. Dittmar, T. Langer, and M. Escobar-Henriques. 2013. Two deubiquitylases act on mitofusin and regulate mitochondrial fusion along independent pathways. *Mol. Cell.* 49:487–498. https://doi.org/10.1016/j.molcel.2012.12.003

Antonny, B., C. Burd, P. De Camilli, E. Chen, O. Daumke, K. Faelber, M. Ford, V.A. Frolov, A. Frost, J.E. Hinshaw, et al. 2016. Membrane fission by dynamin: what we know and what we need to know. *EMBO J.* 35:2270–2284. https://doi.org/10.15252/embj.201694613

Betancourt-Solis, M.A., T. Desai, and J.A. McNew. 2018. The atlastin membrane anchor forms an intramembrane hairpin that does not span the phospholipid bilayer. *J. Biol. Chem.* 293:18514–18524. https://doi.org/10.1074/jbc.RA118.003812

Bian, X., R.W. Klemm, T.Y. Liu, M. Zhang, S. Sun, X. Sui, X. Liu, T.A. Rapoport, and J. Hu. 2011. Structures of the atlastin GTPase provide insight into homotypic fusion of endoplasmic reticulum membranes. *Proc. Natl. Acad. Sci. USA.* 108:3976–3981. https://doi.org/10.1073/pnas.1101643108

Blanquet, P.R. 2000. Casein kinase 2 as a potentially important enzyme in the nervous system. *Prog. Neurobiol.* 60:211–246. https://doi.org/10.1016/S0301-0082(99)00026-X

Bo, T., T. Yamamori, M. Suzuki, Y. Sakai, K. Yamamoto, and O. Inanami. 2018. Calmodulin-dependent protein kinase II (CaMKII) mediates radiation-induced mitochondrial fission by regulating the phosphorylation of dynamin-related protein 1 (Drp1) at serine 616. *Biochem. Biophys. Res. Commun.* 495:1601–1607. https://doi.org/10.1016/j.bbrc.2017.12.012

Brandt, T., L. Cavellini, W. Kühlbrandt, and M.M. Cohen. 2016. A mitofusin-dependent docking ring complex triggers mitochondrial fusion in vitro. *eLife.* 5:e14618. https://doi.org/10.7554/eLife.14618

Byrnes, L.J., and H. Sondermann. 2011. Structural basis for the nucleotide-dependent dimerization of the large G protein atlastin-1/SPG3A. *Proc. Natl. Acad. Sci. USA.* 108:2216–2221. https://doi.org/10.1073/pnas.1012792108

Byrnes, L.J., A. Singh, K. Szeto, N.M. Benvin, J.P. O'Donnell, W.R. Zipfel, and H. Sondermann. 2013. Structural basis for conformational switching and GTP loading of the large G protein atlastin. *EMBO J.* 32:369–384. https://doi.org/10.1038/emboj.2012.353

Cao, H., J. Chen, E.W. Krueger, and M.A. McNiven. 2010. SRC-mediated phosphorylation of dynamin and cortactin regulates the "constitutive" endocytosis of transferrin. *Mol. Cell. Biol.* 30:781–792. https://doi.org/10.1128/MCB.00330-09

Chang, C.R., and C. Blackstone. 2007. Cyclic AMP-dependent protein kinase phosphorylation of Drp1 regulates its GTPase activity and mitochondrial morphology. *J. Biol. Chem.* 282:21583–21587. https://doi.org/10.1074/jbc.C700083200

Chappie, J.S., S. Acharya, Y.W. Liu, M. Leonard, T.J. Pucadyil, and S.L. Schmid. 2009. An intramolecular signaling element that modulates dynamin function in vitro and in vivo. *Mol. Biol. Cell.* 20:3561–3571. https://doi.org/10.1091/mbc.e09-04-0318

Chappie, J.S., S. Acharya, M. Leonard, S.L. Schmid, and F. Dyda. 2010. G domain dimerization controls dynamin's assembly-stimulated GTPase activity. *Nature.* 465:435–440. https://doi.org/10.1038/nature09032

Chen, Q., Y. Xiao, P. Chai, P. Zheng, J. Teng, and J. Chen. 2019. ATL3 is a tubular ER-phagy receptor for GABARAP-mediated selective autophagy. *Curr. Biol.* 29:846–855.e6. https://doi.org/10.1016/j.cub.2019.01.041

Cribbs, J.T., and S. Strack. 2007. Reversible phosphorylation of Drp1 by cyclic AMP-dependent protein kinase and calcineurin regulates mitochondrial fission and cell death. *EMBO Rep.* 8:939–944. https://doi.org/10.1038/sj.embor.7401062

Crooks, G.E., G. Hon, J.M. Chandonia, and S.E. Brenner. 2004. WebLogo: a sequence logo generator. *Genome Res.* 14:1188–1190. https://doi.org/10.1101/gr.849004

Daumke, O., and G.J. Praefcke. 2016. Invited review: Mechanisms of GTP hydrolysis and conformational transitions in the dynamin superfamily. *Biopolymers.* 105:580–593. https://doi.org/10.1002/bip.22855

Emsley, P., B. Lohkamp, W.G. Scott, and K. Cowtan. 2010. Features and development of Coot. *Acta Crystallogr. D Biol. Crystallogr.* 66:486–501. https://doi.org/10.1107/S0907444910007493

Eswaran, J., M. Soundararajan, R. Kumar, and S. Knapp. 2008. UnPAKing the class differences among p21-activated kinases. *Trends Biochem. Sci.* 33:394–403. https://doi.org/10.1016/j.tibs.2008.06.002

Falk, J., M. Rohde, M.M. Bekhite, S. Neugebauer, P. Hemmerich, M. Kiehntopf, T. Deufel, C.A. Hübner, and C. Beetz. 2014. Functional mutation analysis provides evidence for a role of REEP1 in lipid droplet biology. *Hum. Mutat.* 35:497–504. https://doi.org/10.1002/humu.22521

Fassier, C., J.A. Hutt, S. Scholpp, A. Lumsden, B. Giros, F. Nothias, S. Schneider-Maunoury, C. Houart, and J. Hazan. 2010. Zebrafish atlastin controls motility and spinal motor axon architecture via inhibition of the BMP pathway. *Nat. Neurosci.* 13:1380–1387. https://doi.org/10.1038/nn.2662

Faust, M., M. Jung, J. Günther, R. Zimmermann, and M. Montenarh. 2001. Localization of individual subunits of protein kinase CK2 to the endoplasmic reticulum and to the Golgi apparatus. *Mol. Cell. Biochem.* 227:73–80. https://doi.org/10.1023/A:1013129410551

Faust, J.E., T. Desai, A. Verma, I. Ulengin, T.L. Sun, T.J. Moss, M.A. Betancourt-Solis, H.W. Huang, T. Lee, and J.A. McNew. 2015. The Atlastin C-terminal tail is an amphipathic helix that perturbs the bilayer structure during endoplasmic reticulum homotypic fusion. *J. Biol. Chem.* 290:4772–4783. https://doi.org/10.1074/jbc.M114.601823

Fischer, D., M. Schabhüttl, T. Wieland, R. Windhager, T.M. Strom, and M. Auer-Grumbach. 2014. A novel missense mutation confirms ATL3 as a gene for hereditary sensory neuropathy type 1. *Brain.* 137:e286. https://doi.org/10.1093/brain/awu091

Ford, M.G.J., and J.S. Chappie. 2019. The structural biology of the dynamin-related proteins: New insights into a diverse, multitalented family. *Traffic.* 20:717–740. https://doi.org/10.1111/tra.12676

Guelly, C., P.P. Zhu, L. Leonardis, L. Papić, J. Zidar, M. Schabhüttl, H. Strohmaier, J. Weis, T.M. Strom, J. Baets, et al. 2011. Targeted high-throughput sequencing identifies mutations in atlastin-1 as a cause of hereditary sensory neuropathy type I. *Am. J. Hum. Genet.* 88:99–105. https://doi.org/10.1016/j.ajhg.2010.12.003

Hopkins, J.B., R.E. Gillilan, and S. Skou. 2017. *BioXTAS RAW*: improvements to a free open-source program for small-angle X-ray scattering data reduction and analysis. *J. Appl. Cryst.* 50:1545–1553. https://doi.org/10.1107/S1600576717011438

Hornbeck, P.V., B. Zhang, B. Murray, J.M. Kornhauser, V. Latham, and E. Skrzypek. 2015. PhosphoSitePlus, 2014: mutations, PTMs and recalibrations. *Nucleic Acids Res.* 43(D1):D512–D520. https://doi.org/10.1093/nar/gku1267

Hu, J., Y. Shibata, P.P. Zhu, C. Voss, N. Rismanchi, W.A. Prinz, T.A. Rapoport, and C. Blackstone. 2009. A class of dynamin-like GTPases involved in the generation of the tubular ER network. *Cell.* 138:549–561. https://doi.org/10.1016/j.cell.2009.05.025

Hu, X., F. Wu, S. Sun, W. Yu, and J. Hu. 2015. Human atlastin GTPases mediate differentiated fusion of endoplasmic reticulum membranes. *Protein Cell.* 6:307–311. https://doi.org/10.1007/s13238-015-0139-3

Hu, J., Y. Zhang, X. Jiang, H. Zhang, Z. Gao, Y. Li, R. Fu, L. Li, J. Li, H. Cui, and N. Gao. 2019. ROS-mediated activation and mitochondrial translocation of CaMKII contributes to Drp1-dependent mitochondrial fission and apoptosis in triple-negative breast cancer cells by isorhamnetin and chloroquine. *J. Exp. Clin. Cancer Res.* 38:225. https://doi.org/10.1186/s13046-019-1201-4

Jiang, H.C., J.M. Hsu, C.P. Yen, C.C. Chao, R.H. Chen, and C.L. Pan. 2015. Neural activity and CaMKII protect mitochondria from fragmentation in aging Caenorhabditis elegans neurons. *Proc. Natl. Acad. Sci. USA.* 112:8768–8773. https://doi.org/10.1073/pnas.1501831112

Jimah, J.R., and J.E. Hinshaw. 2019. Structural insights into the mechanism of dynamin superfamily proteins. *Trends Cell Biol.* 29:257–273. https://doi.org/10.1016/j.tcb.2018.11.003

Kabsch, W. 2010. Xds. *Acta Crystallogr. D Biol. Crystallogr.* 66:125–132. https://doi.org/10.1107/S0907444909047337

Kar, U.P., H. Dey, and A. Rahaman. 2017. Regulation of dynamin family proteins by post-translational modifications. *J. Biosci.* 42:333–344. https://doi.org/10.1007/s12038-017-9680-y

Kato, S., E. Okamura, T.M. Matsunaga, M. Nakayama, Y. Kawanishi, T. Ichinose, A.H. Iwane, T. Sakamoto, Y. Imoto, M. Ohnuma, et al. 2019. *Cyanidioschyzon merolae* aurora kinase phosphorylates evolutionarily conserved sites on its target to regulate mitochondrial division. *Commun. Biol.* 2:477. https://doi.org/10.1038/s42003-019-0714-x

Kettenbach, A.N., D.K. Schweppe, B.K. Faherty, D. Pechenick, A.A. Pletnev, and S.A. Gerber. 2011. Quantitative phosphoproteomics identifies

substrates and functional modules of Aurora and Polo-like kinase activities in mitotic cells. *Sci. Signal.* 4:rs5. https://doi.org/10.1126/scisignal.2001497

Kinoshita, E., E. Kinoshita-Kikuta, and T. Koike. 2009. Separation and detection of large phosphoproteins using Phos-tag SDS-PAGE. *Nat. Protoc.* 4:1513–1521. https://doi.org/10.1038/nprot.2009.154

Klemm, R.W., J.P. Norton, R.A. Cole, C.S. Li, S.H. Park, M.M. Crane, L. Li, D. Jin, A. Boye-Doe, T.Y. Liu, et al. 2013. A conserved role for atlastin GTPases in regulating lipid droplet size. *Cell Rep.* 3:1465–1475. https://doi.org/10.1016/j.celrep.2013.04.015

Kong, L., K.A. Sochacki, H. Wang, S. Fang, B. Canagarajah, A.D. Kehr, W.J. Rice, M.P. Strub, J.W. Taraska, and J.E. Hinshaw. 2018. Cryo-EM of the dynamin polymer assembled on lipid membrane. *Nature.* 560:258–262. https://doi.org/10.1038/s41586-018-0378-6

Kornak, U., I. Mademan, M. Schinke, M. Voigt, P. Krawitz, J. Hecht, F. Barvencik, T. Schinke, S. Gießelmann, F.T. Beil, et al. 2014. Sensory neuropathy with bone destruction due to a mutation in the membrane-shaping atlastin GTPase 3. *Brain.* 137:683–692. https://doi.org/10.1093/brain/awt357

Krissinel, E., and K. Henrick. 2007. Protein interfaces, surfaces and assemblies service PISA at European Bioinformatics Institute. *J. Mol. Biol.* 372:774–797. https://doi.org/10.1016/j.jmb.2007.05.022

Kucharz, K., and M. Lauritzen. 2018. CaMKII-dependent endoplasmic reticulum fission by whisker stimulation and during cortical spreading depolarization. *Brain.* 141:1049–1062. https://doi.org/10.1093/brain/awy036

Kumar, R., R. Sanawar, X. Li, and F. Li. 2017. Structure, biochemistry, and biology of PAK kinases. *Gene.* 605:20–31. https://doi.org/10.1016/j.gene.2016.12.014

Kuriyan, J., and D. Eisenberg. 2007. The origin of protein interactions and allostery in colocalization. *Nature.* 450:983–990. https://doi.org/10.1038/nature06524

Liang, J.R., E. Lingeman, S. Ahmed, and J.E. Corn. 2018. Atlastins remodel the endoplasmic reticulum for selective autophagy. *J. Cell Biol.* 217:3354–3367. https://doi.org/10.1083/jcb.201804185

Liebschner, D., P.V. Afonine, M.L. Baker, G. Bunkóczi, V.B. Chen, T.I. Croll, B. Hintze, L.W. Hung, S. Jain, A.J. McCoy, et al. 2019. Macromolecular structure determination using X-rays, neutrons and electrons: recent developments in Phenix. *Acta Crystallogr. D Struct. Biol.* 75:861–877. https://doi.org/10.1107/S2059798319011471

Lisman, J., H. Schulman, and H. Cline. 2002. The molecular basis of CaMKII function in synaptic and behavioural memory. *Nat. Rev. Neurosci.* 3:175–190. https://doi.org/10.1038/nrn753

Liu, T.Y., X. Bian, S. Sun, X. Hu, R.W. Klemm, W.A. Prinz, T.A. Rapoport, and J. Hu. 2012. Lipid interaction of the C terminus and association of the transmembrane segments facilitate atlastin-mediated homotypic endoplasmic reticulum fusion. *Proc. Natl. Acad. Sci. USA.* 109:E2146–E2154. https://doi.org/10.1073/pnas.1208385109

Liu, T.Y., X. Bian, F.B. Romano, T. Shemesh, T.A. Rapoport, and J. Hu. 2015. Cis and trans interactions between atlastin molecules during membrane fusion. *Proc. Natl. Acad. Sci. USA.* 112:E1851–E1860. https://doi.org/10.1073/pnas.1504368112

Manalastas-Cantos, K., P.V. Konarev, N.R. Hajizadeh, A.G. Kikhney, M.V. Petoukhov, D.S. Molodenskiy, A. Panjkovich, H.D.T. Mertens, A. Gruzinov, C. Borges, et al. 2021. *ATSAS 3.0*: expanded functionality and new tools for small-angle scattering data analysis. *J. Appl. Cryst.* 54:343–355. https://doi.org/10.1107/S1600576720013412

Mattie, S., J. Riemer, J.G. Wideman, and H.M. McBride. 2018. A new mitofusin topology places the redox-regulated C terminus in the mitochondrial intermembrane space. *J. Cell Biol.* 217:507–515. https://doi.org/10.1083/jcb.201611194

McCullough, S., and J. Lucocq. 2005. Endoplasmic reticulum positioning and partitioning in mitotic HeLa cells. *J. Anat.* 206:415–425. https://doi.org/10.1111/j.1469-7580.2005.00407.x

Monel, B., M.M. Rajah, M.L. Hafirassou, S. Sid Ahmed, J. Burlaud-Gaillard, P.P. Zhu, Q. Nevers, J. Buchrieser, F. Porrot, C. Meunier, et al. 2019. Atlastin endoplasmic reticulum-shaping proteins facilitate Zika virus replication. *J. Virol.* 93:e01047-e19. https://doi.org/10.1128/JVI.01047-19

Morin, A., B. Eisenbraun, J. Key, P.C. Sanschagrin, M.A. Timony, M. Ottaviano, and P. Sliz. 2013. Collaboration gets the most out of software. *eLife.* 2:e01456. https://doi.org/10.7554/eLife.01456

Moss, T.J., C. Andreazza, A. Verma, A. Daga, and J.A. McNew. 2011. Membrane fusion by the GTPase atlastin requires a conserved C-terminal cytoplasmic tail and dimerization through the middle domain. *Proc. Natl. Acad. Sci. USA.* 108:11133–11138. https://doi.org/10.1073/pnas.1105056108

Neufeldt, C.J., M. Cortese, P. Scaturro, B. Cerikan, J.G. Wideman, K. Tabata, T. Moraes, O. Oleksiuk, A. Pichlmair, and R. Bartenschlager. 2019. ER-shaping atlastin proteins act as central hubs to promote flavivirus replication and virion assembly. *Nat. Microbiol.* 4:2416–2429. https://doi.org/10.1038/s41564-019-0586-3

Nikonova, A.S., I. Astsaturov, I.G. Serebriiskii, R.L. Dunbrack Jr., and E.A. Golemis. 2013. Aurora A kinase (AURKA) in normal and pathological cell division. *Cell. Mol. Life Sci.* 70:661–687. https://doi.org/10.1007/s00018-012-1073-7

Nixon-Abell, J., C.J. Obara, A.V. Weigel, D. Li, W.R. Legant, C.S. Xu, H.A. Pasolli, K. Harvey, H.F. Hess, E. Betzig, et al. 2016. Increased spatiotemporal resolution reveals highly dynamic dense tubular matrices in the peripheral ER. *Science.* 354:aaf3928. https://doi.org/10.1126/science.aaf3928

O'Donnell, J.P., R.B. Cooley, C.M. Kelly, K. Miller, O.S. Andersen, R. Rusinova, and H. Sondermann. 2017. Timing and reset mechanism of GTP hydrolysis-driven conformational changes of atlastin. *Structure.* 25:997–1010.e4. https://doi.org/10.1016/j.str.2017.05.007

O'Donnell, J.P., L.J. Byrnes, R.B. Cooley, and H. Sondermann. 2018. A hereditary spastic paraplegia-associated atlastin variant exhibits defective allosteric coupling in the catalytic core. *J. Biol. Chem.* 293:687–700. https://doi.org/10.1074/jbc.RA117.000380

Orso, G., D. Pendin, S. Liu, J. Tosetto, T.J. Moss, J.E. Faust, M. Micaroni, A. Egorova, A. Martinuzzi, J.A. McNew, and A. Daga. 2009. Homotypic fusion of ER membranes requires the dynamin-like GTPase atlastin. *Nature.* 460:978–983. https://doi.org/10.1038/nature08280

Park, S.H., P.P. Zhu, R.L. Parker, and C. Blackstone. 2010. Hereditary spastic paraplegia proteins REEP1, spastin, and atlastin-1 coordinate microtubule interactions with the tubular ER network. *J. Clin. Invest.* 120:1097–1110. https://doi.org/10.1172/JCI40979

Praefcke, G.J., and H.T. McMahon. 2004. The dynamin superfamily: universal membrane tubulation and fission molecules? *Nat. Rev. Mol. Cell Biol.* 5:133–147. https://doi.org/10.1038/nrm1313

Puhka, M., H. Vihinen, M. Joensuu, and E. Jokitalo. 2007. Endoplasmic reticulum remains continuous and undergoes sheet-to-tubule transformation during cell division in mammalian cells. *J. Cell Biol.* 179:895–909. https://doi.org/10.1083/jcb.200705112

Rismanchi, N., C. Soderblom, J. Stadler, P.P. Zhu, and C. Blackstone. 2008. Atlastin GTPases are required for Golgi apparatus and ER morphogenesis. *Hum. Mol. Genet.* 17:1591–1604. https://doi.org/10.1093/hmg/ddn046

Saini, S.G., C. Liu, P. Zhang, and T.H. Lee. 2014. Membrane tethering by the atlastin GTPase depends on GTP hydrolysis but not on forming the cross-over configuration. *Mol. Biol. Cell.* 25:3942–3953. https://doi.org/10.1091/mbc.e14-08-1284

Schneider, C.A., W.S. Rasband, and K.W. Eliceiri. 2012. NIH Image to ImageJ: 25 years of image analysis. *Nat. Methods.* 9:671–675. https://doi.org/10.1038/nmeth.2089

Shen, W., B. Liu, Z. Liu, J. Feng, C. Liu, and X. Kong. 2017. Host protein atlastin-1 promotes human immunodeficiency virus (HIV-1) replication. *Virol. Sin.* 32:338–341. https://doi.org/10.1007/s12250-017-3998-3

Shutt, T., M. Geoffrion, R. Milne, and H.M. McBride. 2012. The intracellular redox state is a core determinant of mitochondrial fusion. *EMBO Rep.* 13:909–915. https://doi.org/10.1038/embor.2012.128

Smillie, K.J., and M.A. Cousin. 2005. Dynamin I phosphorylation and the control of synaptic vesicle endocytosis. *Biochem. Soc. Symp.* 72:87–97. https://doi.org/10.1042/bss0720087

Srinivasan, S., C.J. Burckhardt, M. Bhave, Z. Chen, P.H. Chen, X. Wang, G. Danuser, and S.L. Schmid. 2018. A noncanonical role for dynamin-1 in regulating early stages of clathrin-mediated endocytosis in non-neuronal cells. *PLoS Biol.* 16:e2005377. https://doi.org/10.1371/journal.pbio.2005377

Steiner, B., A.L. Swart, A. Welin, S. Weber, N. Personnic, A. Kaech, C. Freyre, U. Ziegler, R.W. Klemm, and H. Hilbi. 2017. ER remodeling by the large GTPase atlastin promotes vacuolar growth of *Legionella pneumophila*. *EMBO Rep.* 18:1817–1836. https://doi.org/10.15252/embr.201743903

Summerville, J.B., J.F. Faust, E. Fan, D. Pendin, A. Daga, J. Formella, M. Stern, and J.A. McNew. 2016. The effects of ER morphology on synaptic structure and function in Drosophila melanogaster. *J. Cell Sci.* 129:1635–1648.

Sun, J., N. Movahed, and H. Zheng. 2020. LUNAPARK is an E3 ligase that mediates degradation of ROOT HAIR DEFECTIVE3 to maintain a tubular ER network in Arabidopsis. *Plant Cell.* 32:2964–2978. https://doi.org/10.1105/tpc.18.00937

Terasaki, M., L.B. Chen, and K. Fujiwara. 1986. Microtubules and the endoplasmic reticulum are highly interdependent structures. *J. Cell Biol.* 103:1557–1568. https://doi.org/10.1083/jcb.103.4.1557

Terwilliger, T.C., P.D. Adams, R.J. Read, A.J. McCoy, N.W. Moriarty, R.W. Grosse-Kunstleve, P.V. Afonine, P.H. Zwart, and L.W. Hung. 2009. Decision-making in structure solution using Bayesian estimates of map quality: the PHENIX AutoSol wizard. *Acta Crystallogr. D Biol. Crystallogr.* 65:582–601. https://doi.org/10.1107/S0907444909012098

Tuma, P.L., and C.A. Collins. 1994. Activation of dynamin GTPase is a result of positive cooperativity. *J. Biol. Chem.* 269:30842–30847. https://doi.org/10.1016/S0021-9258(18)47358-9

Turnham, R.E., and J.D. Scott. 2016. Protein kinase A catalytic subunit isoform PRKACA; History, function and physiology. *Gene.* 577:101–108. https://doi.org/10.1016/j.gene.2015.11.052

Ueda, H., E. Yokota, K. Kuwata, N. Kutsuna, S. Mano, T. Shimada, K. Tamura, G. Stefano, Y. Fukao, F. Brandizzi, et al. 2016. Phosphorylation of the C terminus of RHD3 has a critical role in homotypic ER membrane fusion in Arabidopsis. *Plant Physiol.* 170:867–880. https://doi.org/10.1104/pp.15.01172

Venerando, A., M. Ruzzene, and L.A. Pinna. 2014. Casein kinase: the triple meaning of a misnomer. *Biochem. J.* 460:141–156. https://doi.org/10.1042/BJ20140178

Wang, S., F.B. Romano, C.M. Field, T.J. Mitchison, and T.A. Rapoport. 2013. Multiple mechanisms determine ER network morphology during the cell cycle in Xenopus egg extracts. *J. Cell Biol.* 203:801–814. https://doi.org/10.1083/jcb.201308001

Warnock, D.E., J.E. Hinshaw, and S.L. Schmid. 1996. Dynamin self-assembly stimulates its GTPase activity. *J. Biol. Chem.* 271:22310–22314. https://doi.org/10.1074/jbc.271.37.22310

Wu, F., X. Hu, X. Bian, X. Liu, and J. Hu. 2015. Comparison of human and Drosophila atlastin GTPases. *Protein Cell.* 6:139–146. https://doi.org/10.1007/s13238-014-0118-0

Xu, S., P. Wang, H. Zhang, G. Gong, N. Gutierrez Cortes, W. Zhu, Y. Yoon, R. Tian, and W. Wang. 2016. CaMKII induces permeability transition through Drp1 phosphorylation during chronic β-AR stimulation. *Nat. Commun.* 7:13189. https://doi.org/10.1038/ncomms13189

Zhao, J., and P. Hedera. 2013. Hereditary spastic paraplegia-causing mutations in atlastin-1 interfere with BMPRII trafficking. *Mol. Cell. Neurosci.* 52:87–96. https://doi.org/10.1016/j.mcn.2012.10.005

Zhao, X., D. Alvarado, S. Rainier, R. Lemons, P. Hedera, C.H. Weber, T. Tukel, M. Apak, T. Heiman-Patterson, L. Ming, et al. 2001. Mutations in a newly identified GTPase gene cause autosomal dominant hereditary spastic paraplegia. *Nat. Genet.* 29:326–331. https://doi.org/10.1038/ng758

Zhao, G., P.P. Zhu, B. Renvoisé, L. Maldonado-Báez, S.H. Park, and C. Blackstone. 2016. Mammalian knock out cells reveal prominent roles for atlastin GTPases in ER network morphology. *Exp. Cell Res.* 349:32–44. https://doi.org/10.1016/j.yexcr.2016.09.015

Zhao, Y., Z. Feng, Y. Zou, and Y. Liu. 2020. The E3 Ubiquitin Ligase SYVN1 Ubiquitinates Atlastins to Remodel the Endoplasmic Reticulum Network. *iScience.* 23:101494. https://doi.org/10.1016/j.isci.2020.101494

Zhou, W., K.H. Chen, W. Cao, J. Zeng, H. Liao, L. Zhao, and X. Guo. 2010. Mutation of the protein kinase A phosphorylation site influences the anti-proliferative activity of mitofusin 2. *Atherosclerosis.* 211:216–223. https://doi.org/10.1016/j.atherosclerosis.2010.02.012

Zhu, P.P., A. Patterson, B. Lavoie, J. Stadler, M. Shoeb, R. Patel, and C. Blackstone. 2003. Cellular localization, oligomerization, and membrane association of the hereditary spastic paraplegia 3A (SPG3A) protein atlastin. *J. Biol. Chem.* 278:49063–49071. https://doi.org/10.1074/jbc.M306702200

Zurek, N., L. Sparks, and G. Voeltz. 2011. Reticulon short hairpin transmembrane domains are used to shape ER tubules. *Traffic.* 12:28–41. https://doi.org/10.1111/j.1600-0854.2010.01134.x

Supplemental material

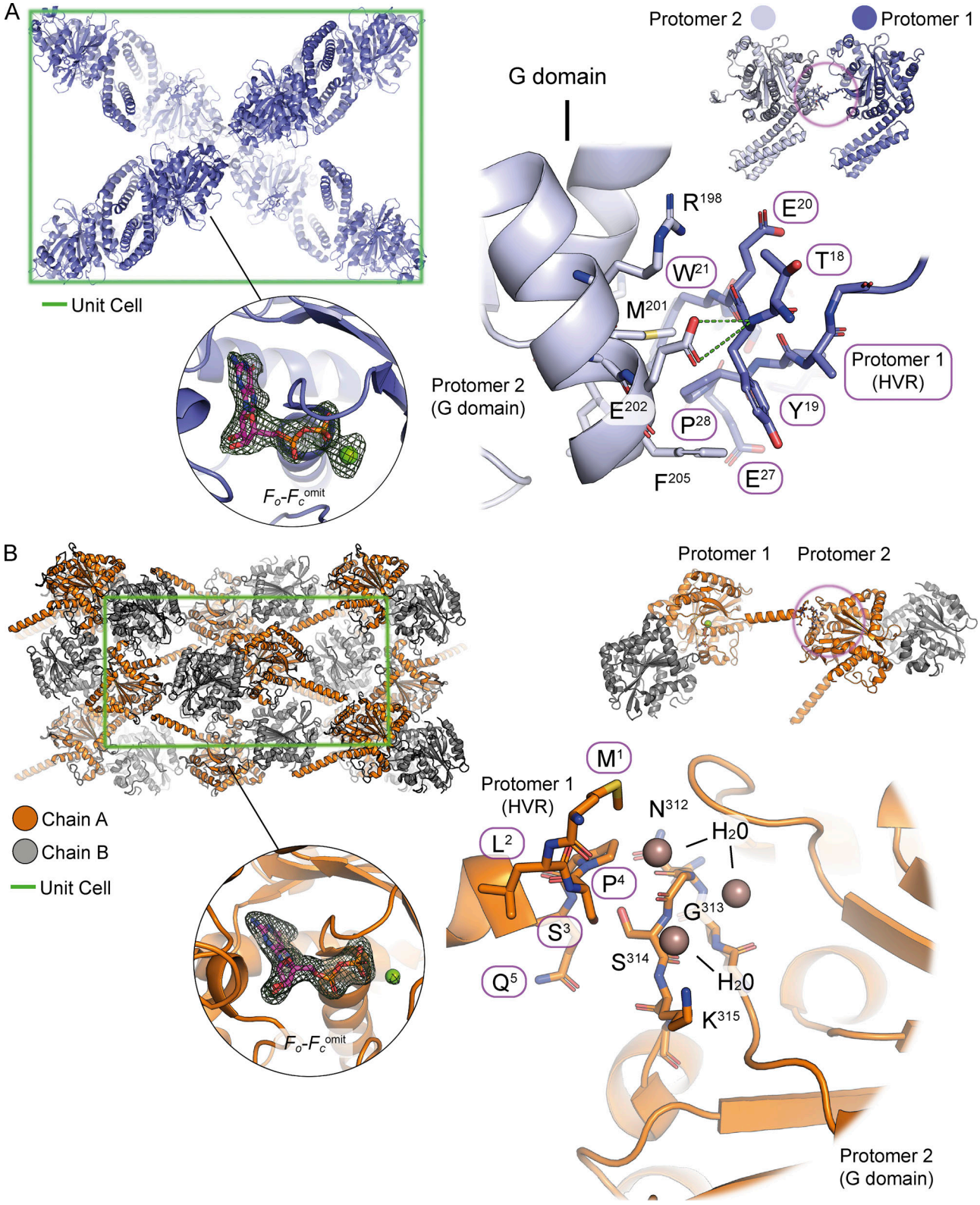

Figure S1. **Molecular details of crystal packing, HVR interactions, and ligand density. (A)** Crystal structure of ATL1. A unit cell of the crystal is shown in the top left corner. The inset below shows an F_o-F_c omit map contoured at 3 σ for the bound nucleotide (GDP) and magnesium ion. The left panel shows the interaction interface between the HVR of one molecule with the G domain of an adjacent protomer in the crystal. At the center of the interface is a hydrophobic interaction of P^{28} of the HVR F^{205} and M^{201} of the G domain. In addition, E202 interacts with the peptide backbone of the HVR. **(B)** Crystal structure of ATL3. The presentation follows details mentioned in A. The interaction between the tip of the helix formed by the HVR motif and an adjacent G domain is minimal.

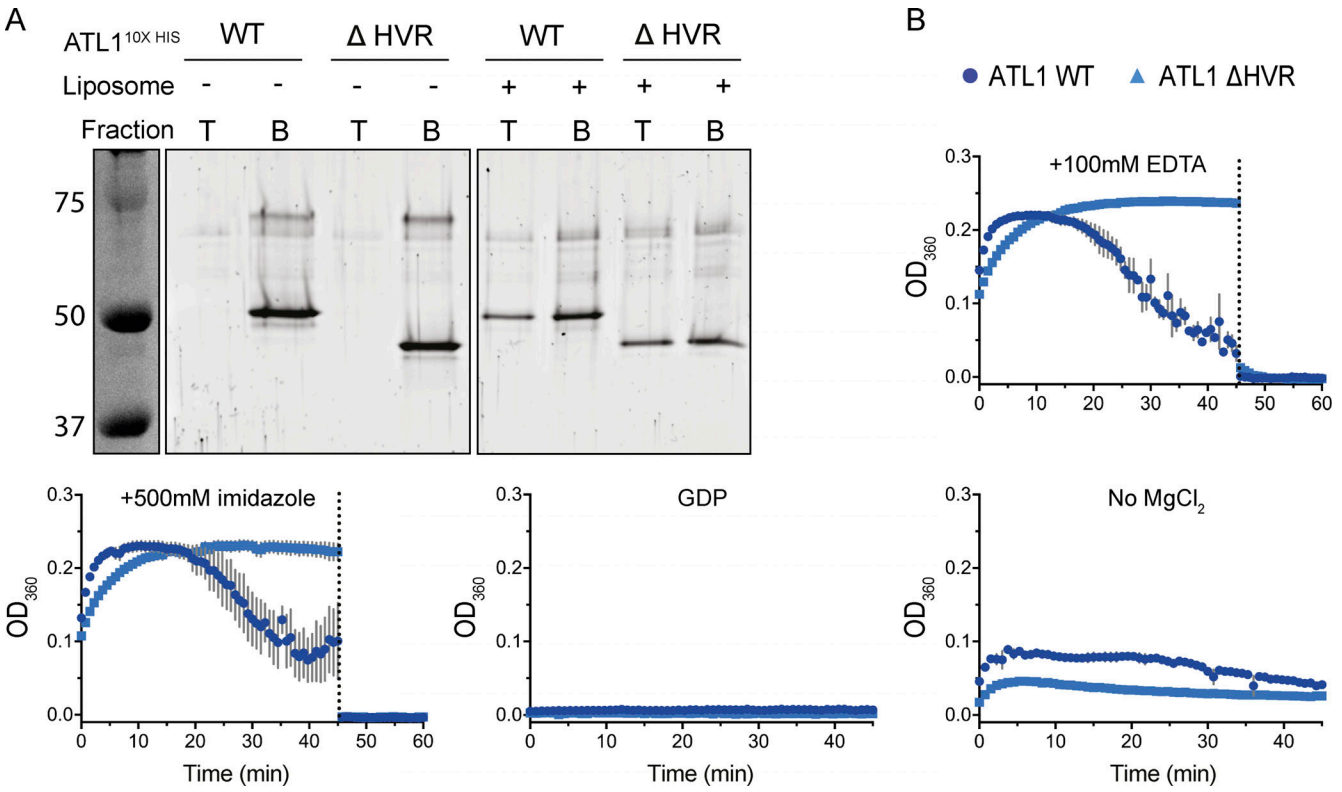

Figure S2. **Vesicle tethering controls. (A)** Flotation assay using Nycodenz with 1 µM ATL1^{10xHIS} WT or ΔHVR catalytic core fragment in the presence (right two panes) or absence (left two panes) or lipids containing 1% molar ratio of Ni^{2+}-NTA–modified lipids. Top ("T") and bottom ("B") fractions were analyzed by SDS-PAGE and stained with SYPRO Ruby gel stain. The protein ladder on the left is labeled with molecular weights in kilodaltons and was stained with Coomassie stain. **(B)** Controls for tethering reactions in Fig. 3 performed with 1 µM ATL1^{10xHIS} and either addition of 100 mM EDTA or 500 mM imidazole at 45 min, or in the absence of $MgCl_2$ or presence of 2 mM GDP. Each data point represents the average of triplicate reactions (n = 3), with error bars in gray representing SD.

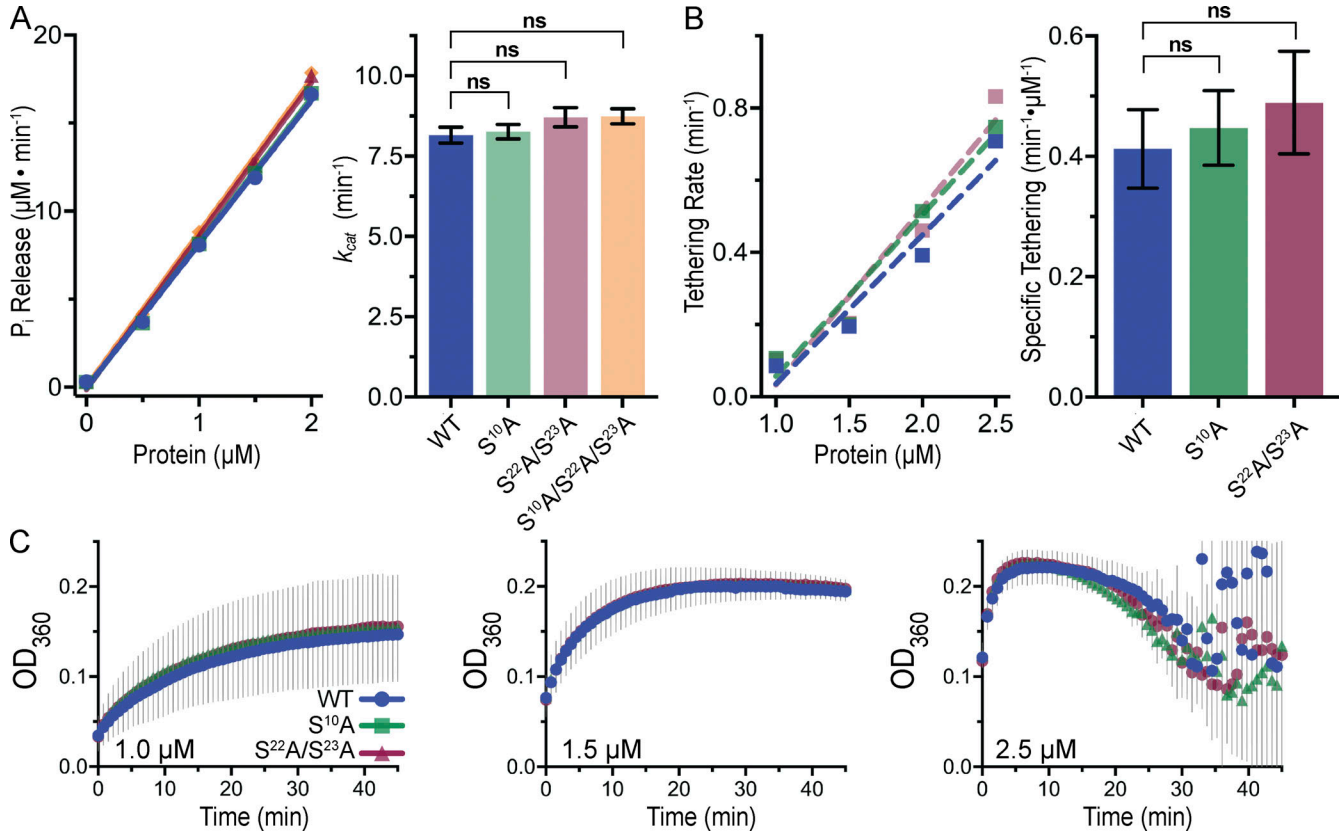

Figure S3. **Phosphate release and tethering kinetics for ATL1 S-to-A mutants. (A)** Left: Phosphate release kinetics of the catalytic core of ATL1 WT (blue), $S^{10}A$ (light green), $S^{22}A/S^{23}A$ (pink), and $S^{10}A/S^{22}A/S^{23}A$ (light orange) in units of μM P_i released per minute at increasing protein concentration (0–2 μM). All reactions were performed in triplicate with two technical replicates (n = 6). Right: Apparent turnover rates for each mutant. Experimental set-up and analysis as in Fig. 5 A. Statistical significance compared with ATL1 WT was determined using an unpaired, two-tailed t test, assuming normal data distribution. **(B)** Tethering rate analysis as described in Fig. 5 B. **(C)** Tethering reactions for ATL1^{10xHIS} WT (blue), $S^{10}A$ (light green), and $S^{22}A/S^{23}A$ (pink) measured at OD_{360} across 45-min reactions, with the first 10 min inset to the right. Each experimental condition was performed in triplicate with two biological replicates (n = 6).

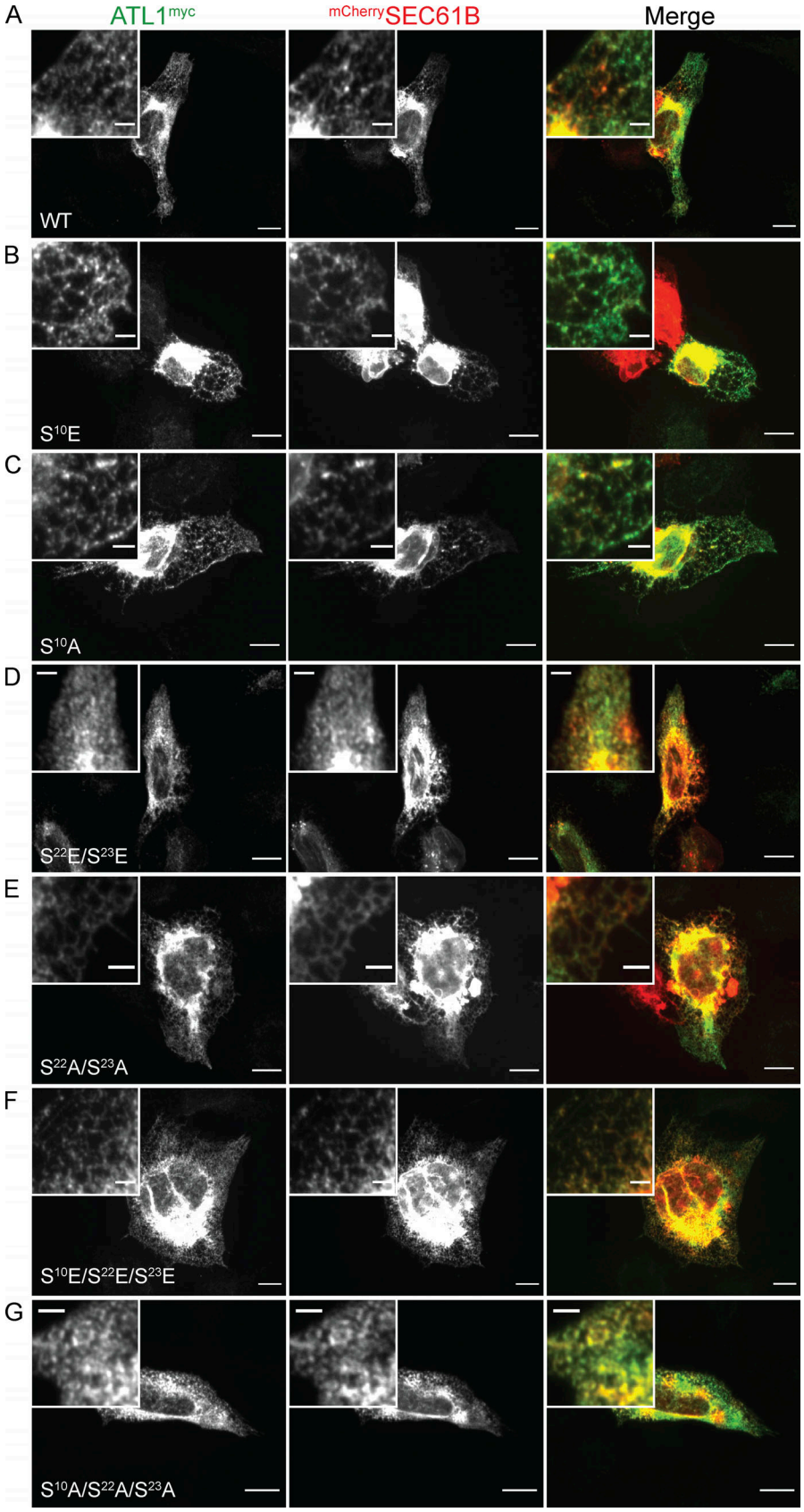

Figure S4. **ER localization of ATL1 mutants.** ATL1 WT, ΔHVR, $S^{10}E$, $S^{10}A$, $S^{22}E/S^{23}E$, $S^{22}A/S^{23}A$, $S^{10}E/S^{22}E/S^{23}E$, and $S^{10}A/S^{22}A/S^{23}A$. **(A–G)** $ATL1^{myc}$ constructs used in Fig. 6 transiently cotransfected with mCherry-SEC61β in U2OS cells. Cells were processed for immunofluorescence using α-c-myc antibodies, with $ATL1^{myc}$ mutants shown in green and SEC61β in red. Main image scale bar = 10 µM; inset scale image scale bar = 2.5 µm.

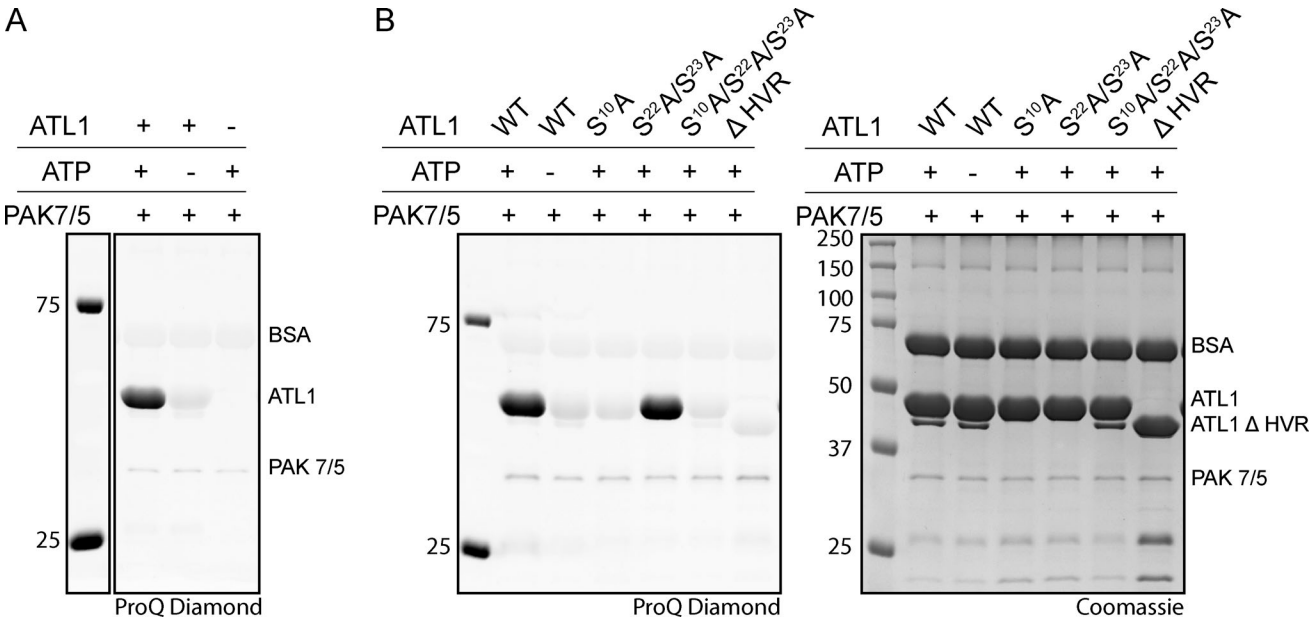

Figure S5. **In vitro phosphorylation controls and gel staining. (A)** ProQ Diamond phosphoprotein-stained SDS-PAGE analysis of kinase reaction with PAK7/5 ± recombinant ATL1 substrate and ± ATP. BSA was included in the reaction buffer. Bands of interest labeled on right of the gel: BSA (69.3 kD), the catalytic core of ATL1 (52.8 kD), and PAK7/5 (36.7 kD). Molecular weights labeled on the left in kilodaltons. **(B)** Follow-up kinase reactions from A corresponding to Fig. 8, B–F. Experimental set-up as in A except point mutants and HVR deletion mutant of ATL1 were used as the substrates. Reactions analyzed by SDS-PAGE stained with phosphoprotein-specific ProQ Diamond (left) and Coomassie (right). Bands of interest labeled on the right as in A, with the addition of ΔHVR ATL1 (48.9 kD). Molecular weights as indicated on the left in kilodaltons.